Molecular diffusion of stable water isotopes in polar firn as a proxy for past temperatures

Christian Holme[†*a], Vasileios Gkinis[*a], and Bo M. Vinther[a]

[a]The Niels Bohr Institute, Centre for Ice and Climate, Juliane Maries Vej 30, 2100 Copenhagen, Denmark

[†]Corresponding author: christian.holme@nbi.ku.dk (C. Holme)

[*]The two authors contributed equally to this work

Abstract

Polar precipitation archived in ice caps contains information on past temperature conditions. Such information can be retrieved by measuring the water isotopic signals of $\delta^{18}O$ and δD in ice cores. These signals have been attenuated during densification due to molecular diffusion in the firn column, where the magnitude of the diffusion is isotopologoue specific and temperature dependent. By utilizing the differential diffusion signal, dual isotope measurements of $\delta^{18}O$ and δD enable multiple temperature reconstruction techniques. This study assesses how well six different methods can be used to reconstruct past surface temperatures from the diffusion-based temperature proxies. Two of the methods are based on the single diffusion lengths of $\delta^{18}O$ and δD, three of the methods employ the differential diffusion signal, while the last uses the ratio between the single diffusion lengths. All techniques are tested on synthetic data in order to evaluate their accuracy and precision. In addition, a benchmark test is applied to thirteen high resolution data sets from Greenland and Antarctica, which represent a broad range of mean annual surface temperatures and accumulation rates. The presented methods are found to accurately reconstruct the temperatures of the synthetic data, and the estimated temperatures are shown to be unbiased. Both the benchmark test and the synthetic data test demonstrate that the most precise reconstructions are obtained when using the single isotope diffusion lengths, with precisions around $1.0\,^{\circ}C$. In the benchmark test, the single isotope diffusion lengths are also found to reconstruct consistent temperatures with a root-mean-square-deviation of $0.7\,^{\circ}C$. The techniques employing the differential diffusion signals are more uncertain, where the most precise method has a precision of $1.9\,^{\circ}C$. The diffusion length ratio method is the least precise with a precision of $13.7\,^{\circ}C$. The absolute temperature estimates from this method are also shown to be highly sensitive to the choice of fractionation factor parameterization. From the combined analyses of the water isotope diffusion methods of the synthetic data and ice core data, this

study demonstrates that methods based on the single isotope diffusion lengths result in the most accurate and precise estimates of past temperatures.

Keywords

Holocene, paleoclimatology, ice cores, isotope geochemistry, stable isotopes, diffusion, Greenland, Antarctica.

1 INTRODUCTION

Polar precipitation stored for thousands of years in the ice caps of Greenland and Antarctica contains unique information on past climatic conditions. The isotopic composition of polar ice commonly expressed through the δ notation has been shown to work as a direct proxy of the relative depletion of a water vapor mass in its journey from the evaporation site to the place where condensation takes place (Epstein et al. 1951, Mook 2000). Additionally, for modern times, it shows a good correlation with the temperature of the cloud at the time of precipitation (Dansgaard 1954, 1964) and as a result it has been proposed and used as a proxy of past temperatures (Jouzel & Merlivat 1984, Jouzel et al. 1997, Johnsen et al. 2001).

The use of the isotopic paleothermometer presents some notable limitations. The constant linear relationship between $\delta^{18}O$ and temperature commonly referred to as the "spatial slope" may hold for present conditions, but studies based on borehole temperature reconstruction (Cuffey et al. 1994, Johnsen et al. 1995) as well as the thermal fractionation of the $\delta^{15}N$ signal in polar firn (Severinghaus et al. 1998, Severinghaus & Brook 1999) have independently underlined the inaccuracy of the spatial isotope slope when it is extrapolated to past climatic conditions. Even though qualitatively the $\delta^{18}O$ signal comprises past temperature information, it fails to provide a quantitative picture on the magnitudes of past climatic changes.

Johnsen (1977), Whillans & Grootes (1985) and Johnsen et al. (2000) set the foundations for the quantitative description of the diffusive processes the water isotopic signal undergoes in the porous firn layer from the time of deposition until pore close–off. Even though the main purpose of Johnsen et al. (2000) was to investigate how to reconstruct the part of the signal that was attenuated during the diffusive processes, the authors make a clear reference to the possibility of using the assessment of the diffusive rates as a proxy for past firn temperatures.

The temperature reconstruction method based on isotope firn diffusion requires data of high resolution. Moreover, if one would like to look into the differential diffusion signal, datasets of both $\delta^{18}O$ and δD are required. Such data sets have until recently not been easy to obtain especially due to the challenging nature of the δD analysis (Bigeleisen et al. 1952, Vaughn et al. 1998). With the advent of present commercial

high–accuracy, high–precision Infra-Red spectrometers (Crosson 2008, Brand et al. 2009), simultaneous measurements of δ^{18}O and δD have become easier to obtain. Coupling of these instruments to Continuous Flow Analysis systems (Gkinis et al. 2011, Emanuelsson et al. 2015, Jones et al. 2017) can also result in measurements of ultra–high resolution, a necessary condition for accurate temperature reconstructions based on water isotope diffusion.

A number of existing works have presented past firn temperature reconstructions based on water isotope diffusion. Simonsen et al. (2011) and Gkinis et al. (2014) used high resolution isotopic datasets from the NorthGRIP ice core (NGRIP members 2004). The first study makes use of the differential diffusion signal, utilizing spectral estimates of high–resolution dual δ^{18}O and δD datasets covering the GS–1 and GI–1 periods in the NorthGRIP ice core (Rasmussen et al. 2014). The second study presents a combined temperature and accumulation history of the past 16,000 years based on the power spectral density (**PSD** hereafter) signals of high resolution δ^{18}O measurements of the NorthGRIP ice core. More recently, van der Wel et al. (2015) introduced a slightly different approach for reconstructing the differential diffusion signal and testing it on dual δ^{18}O, δD high resolution data from the EDML ice core (Oerter et al. 2004). By artificially forward–diffusing the δD signal the authors estimate differential diffusion rates by maximizing the correlation between the δ^{18}O and δD signal.

In this work we attempt to look into all different varieties of temperature diffusion reconstruction techniques and assess their performance. We use synthetic, as well as real ice core data sets that represent Holocene conditions from a variety of drilling sites on Greenland and Antarctica. Our objective is to use data sections that originate from parts of the core as close to present day as possible. By doing this we aim to minimize possible uncertainties and biases in the ice flow thinning adjustment that is required for temperature interpretation of the diffusion rate estimates. Such a bias has been shown to exist for the NorthGRIP ice core (Gkinis et al. 2014), most likely due to the Dansgaard & Johnsen (1969) ice flow model overestimating the past accumulation rates for the site. In order to include as much data as possible, approximately half of the datasets used here have an age of 9-10 ka. This age coincides with the timing of the early Holocene Climate Optimum around 5-9 ka (**HCO** hereafter). For Greenlandic drill sites, temperatures were up to $3\,^{\circ}$C warmer than present day during the HCO (Dahl-Jensen et al. 1998). Another aspect of this study is that it uses water isotopic data sets of δ^{18}O and δD measured using different analytical techniques, namely Isotope Ratio Mass Spectroscopy (**IRMS** hereafter) as well as Cavity Ring Down Spectroscopy (**CRDS** hereafter). Two of the data sets presented here were obtained using Continuous Flow Analysis (**CFA** hereafter) systems tailored for water isotopic analysis (Gkinis et al. 2011). All data sections are characterized by a very high sampling resolution typically of $5\,\mathrm{cm}$ or better.

2 DIFFUSION OF WATER ISOTOPE SIGNALS IN FIRN

95 The main focus of this section is to outline the various temperature reconstruction techniques that

96 can be employed for paleotemperature reconstructions. The fundamentals of isotope diffusion theory

97 are also presented. In order to avoid significant overlap with previously published works e.g. Johnsen

98 (1977), Johnsen et al. (2000), Simonsen et al. (2011), Gkinis et al. (2014), van der Wel et al. (2015)

99 we occasionally point the reader to any of the latter or/and refer to specific sections in the Appendix.

100 We exemplify and illustrate the use of various techniques using synthetic data prepared such that they

101 resemble two representative regimes of ice coring sites on the Greenland summit and the East Antarctic

102 Plateau.

103

104 The porous medium of the top $60-80\,\mathrm{m}$ of firn allows for a molecular diffusion process that attenuates

105 the water isotope signal from the time of deposition until pore close–off. The process takes place in the

106 vapor phase and it can be described by Fick's second law as (assuming that the water isotope ratio signal

107 (δ) approximates the concentration):

$$\frac{\partial \delta}{\partial t} = D\left(t\right)\frac{\partial^2 \delta}{\partial z^2} - \dot{\varepsilon}_z\left(t\right) z\,\frac{\partial \delta}{\partial z} \tag{2.1}$$

108 where $D\left(t\right)$ is the diffusivity coefficient, $\dot{\varepsilon}_z\left(t\right)$ the vertical strain rate and z is the vertical axis of a

109 coordinate system, with its origin being fixed within the considered layer. The attenuation of the isotopic

110 signal results in loss of information. However the dependence of $\dot{\varepsilon}_z\left(t\right)$ and $D\left(t\right)$ on temperature and

111 accumulation presents the possibility of using the process as a tool to infer these two paleoclimatic

112 parameters. A solution to Eq. 2.1 can be given by the convolution of the initial isotopic profile δ' with

113 a Gaussian filter $\mathcal{G}$ as:

$$\delta\left(z\right) = \mathcal{S}\left(z\right)\left[\delta'\left(z\right) * \mathcal{G}\left(z\right)\right] \tag{2.2}$$

114 where the Gaussian filter is described as:

$$\mathcal{G}\left(z\right) = \frac{1}{\sigma\sqrt{2\pi}}\,e^{\frac{-z^2}{2\sigma^2}}\ \ , \tag{2.3}$$

115 and $\mathcal{S}$ is the total thinning of the layer at depth z described by

$$\mathcal{S}\left(z\right) = e^{\int_0^z \dot{\varepsilon}_z(z')\mathrm{d}z'}\ \ . \tag{2.4}$$

116 In Eq. 2.3, the standard deviation term σ^2 represents the average displacement of a water molecule along

117 the z–axis and is commonly referred to as the diffusion length. The σ^2 quantity is a direct measure of

118 diffusion and its accurate estimate is critical to any attempt of reconstructing temperatures that are based

119 on the isotope diffusion thermometer. The diffusion length is directly related to the diffusivity coefficient

₁₂₀ and the strain rate (as the strain rate is approximately proportional to the densification rate in the firn

₁₂₁ column) and it can therefore be regarded as a measure of firn temperature as well as accumulation rate.

₁₂₂ The differential equation describing the evolution of σ^2 with time is given by (Johnsen 1977):

$$\frac{\mathrm{d}\sigma^2}{\mathrm{d}t} - 2\dot{\varepsilon}_z(t)\,\sigma^2 = 2D(t) \quad . \tag{2.5}$$

₁₂₃ In the case of firn the following approximation can be made for the strain rate:

$$\dot{\varepsilon}_z(t) \approx -\frac{\mathrm{d}\rho}{\mathrm{d}t}\,\frac{1}{\rho}, \tag{2.6}$$

₁₂₄ with ρ representing the density. Then for the firn column, Eq. 2.5 can be solved hereby yielding a solution

₁₂₅ for σ^2:

$$\sigma^2(\rho) = \frac{1}{\rho^2} \int_{\rho_o}^{\rho} 2\rho^2 \left(\frac{\mathrm{d}\rho}{\mathrm{d}t}\right)^{-1} D(\rho)\,\mathrm{d}\rho, \tag{2.7}$$

₁₂₆ where ρ_o is the surface density. Under the assumption that the diffusivity coefficient $D(\rho)$ and the

₁₂₇ densification rate $\frac{\mathrm{d}\rho}{\mathrm{d}t}$ are known, integration from surface density ρ_o to the close–off density ρ_{co} can be

₁₂₈ performed yielding a model based estimate for the diffusion length. In this work we make use of the

₁₂₉ Herron–Langway densification model (**H–L hereafter**) and the diffusivity rate parametrization introduced

₁₃₀ by Johnsen et al. (2000) (see Appendix A). $\frac{\mathrm{d}\rho}{\mathrm{d}t}$ depends on temperature and overburden pressure and $D(\rho)$

₁₃₁ depends on temperature and firn connectivity. The dependence of the diffusion length on temperature and

₁₃₂ accumulation provide the basis for the use of firn diffusion as a proxy of temperature or accumulation. In

₁₃₃ order to reconstruct the temperature, the accumulation rate is assumed known and vice versa. In the firn

₁₃₄ diffusion model, a seasonal temperature signal that propagates down in the firn is included (see Appendix

₁₃₅ B). The seasonal temperature variation affects the firn diffusion length nonlinearly in the upper $10-12\,\mathrm{m}$

₁₃₆ due to the saturation vapor pressure's exponential dependence on temperature.

₁₃₇ In Fig. 2.1 we evaluate Eq. 2.7 for all three isotopic ratios of water (δ^{18}O, δ^{17}O, δD) using boundary

₁₃₈ conditions characteristic of ice core sites from central Greenland and the East Antarctic Ice Cap. We ac-

₁₃₉ knowledge that high resolution measurements of δ^{17}O currently are unavailable, but synthetic δ^{17}O signals

₁₄₀ have been evaluated in order to demonstrate its potential as a diffusion-based temperature proxy. In Fig.

₁₄₁ 2.1, the transition between zone 1 and zone 2 densification (at the critical density $\rho_c = 550\,\mathrm{kgm^{-3}}$)

₁₄₂ is evident as a kink in both the densification and diffusion model. For the first case we consider cold

₁₄₃ and dry conditions (case **A** hereafter) representative of Antarctic ice coring sites (e.g. Dome C, Vostok)

₁₄₄ with a surface temperature $T_{\mathrm{sur}} = -55\,^\circ\mathrm{C}$ and annual accumulation $A = 0.032\ \mathrm{myr^{-1}}\,\mathrm{ice\,eq}$. For the

₁₄₅ second case we consider relatively warm and humid conditions (case **B** hereafter) representative of central

₁₄₆ Greenlandic ice coring sites (e.g. GISP2, GRIP, NorthGRIP) with a surface temperature $T_{\mathrm{sur}} = -29\,^\circ\mathrm{C}$

₁₄₇ and annual accumulation $A = 0.22\ \mathrm{myr^{-1}}\,\mathrm{ice\,eq}$. In this study, drill sites that have a vast amount of
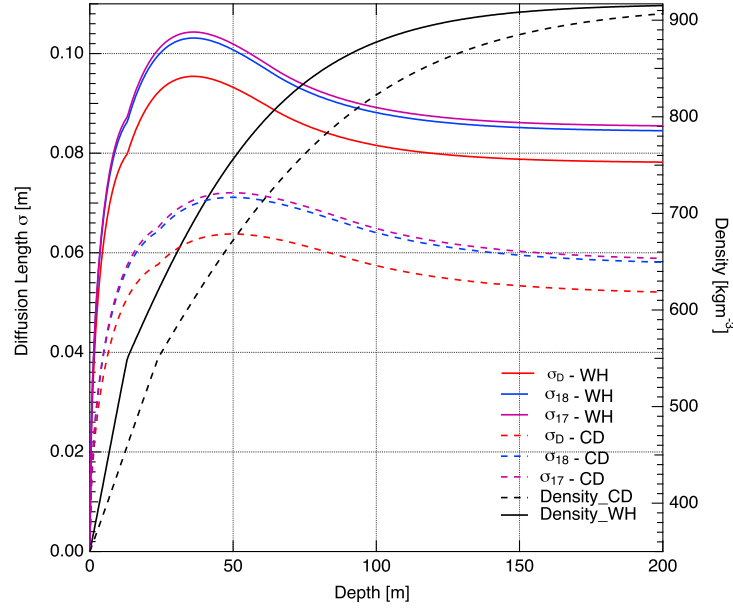
Figure 2.1: Diffusion length and density profiles (black) for case A (solid curves: $T_{\mathrm{sur}} = -29\,^{\circ}\mathrm{C}$, $A = 0.22\ \mathrm{myr}^{-1}$) and B (dashed lines: $T_{\mathrm{sur}} = -55\,^{\circ}\mathrm{C}$, $A = 0.032\ \mathrm{myr}^{-1}$). The increase in diffusion of the $\delta^{18}\mathrm{O}$ (blue color), $\delta^{17}\mathrm{O}$ (purple color) and $\delta\mathrm{D}$ (red color) isotope signals are partially due to the compaction of the firn which moves the ice closer together.

melt layers have been excluded. Melt layers will stop the mixing between the air in the firn and the surrounding atmosphere earlier than the natural densification process. This will result in a small diffusion length. While performing temperature reconstructions, the small diffusion length will falsely result in a low temperature even though the climate was warm. It is therefore difficult to get an accurate estimate of the firn diffusion length if the drill sites have too warm surface temperatures.

3 ISOTOPE DIFFUSION IN THE SOLID PHASE

Below the close-off depth, diffusion occurs in solid ice driven by the isotopic gradients within the lattice of the ice crystals. This process is orders of magnitude slower than firn diffusion. Several studies exist that deal with the estimate of the diffusivity coefficient in ice (Itagaki 1964, Blicks et al. 1966, Delibaltas et al. 1966, Ramseier 1967, Livingston et al. 1997). The differences resulting from the various diffusivity coefficients are small and certainly negligible for the case of our study where the influence of solid ice diffusion is practically negligible. As done before by other similar firn diffusion studies
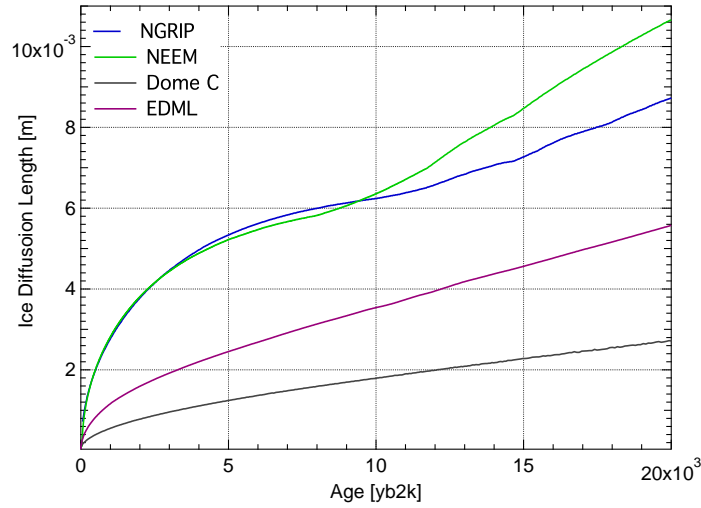
Figure 3.1: The ice diffusion length plotted with respect to age [b2k] for some selected sites from Greenland (NGRIP and NEEM) and Antarctica (Dome C and EDML). For the Greenlandic ice cores, ice diffusion starts increasing rapidly as a layer moves closer to the warm bedrock.

160 (Johnsen et al. 2000, Simonsen et al. 2011, Gkinis et al. 2014) we make use of the parametrization given
161 in Ramseier (1967) as:

$$D_{\mathrm{ice}} = 9.2 \cdot 10^{-4} \cdot \exp\left(-\frac{7186}{T}\right) \mathrm{m^2 s^{-1}}. \tag{3.1}$$

162 Assuming that a depth–age scale as well as a thinning function are available for the ice core a solution
163 for the ice diffusion length is given by (see Appendix C for details):

$$\sigma_{\mathrm{ice}}^2(t') = S(t')^2 \int_0^{t'} 2D_{\mathrm{ice}}(t)\, S(t)^{-2}\ \mathrm{d}t. \tag{3.2}$$

164 In Fig. 3.1 we have calculated ice diffusion lengths for four different cores (NGRIP, NEEM, Dome C,
165 EDML). For the calculation of the diffusivities we have used high precision measurements of borehole
166 temperature profiles and assumed a steady state condition. As it can be seen, for the low temperature/low
167 accumulation sites of Dome C and EDML, σ_{ice} is lower. As the temperature of the ice increases closer
168 to the bedrock σ_{ice} increases monotonically. For the special case of the Dome C core (with a bottom age
169 exceeding 800,000 years), σ_{ice} reaches values as high as 15 cm.

171 *4.1 The single isotopologue diffusion*

172   The simplest implementation of the water isotope diffusion thermometer focuses on the assessment of

173 the diffusion rates of one isotopologue in firn. Implementation of Eq. 2.7, yields diffusion length values

174 from surface to close–off and below with ice thinning disregarded for now.

175   A fundamental property of the convolution operation is that it is equivalent to multiplication in the

176 frequency domain. The transfer function for the diffusion process will be given by the Fourier transform

177 of the Gaussian filter that will itself be a Gaussian function described by (Abramowitz & Stegun 1964,

178 Gkinis et al. 2014):

$$\mathfrak{F}[\mathcal{G}(z)] = \hat{\mathcal{G}} = e^{\frac{-k^2\sigma^2}{2}} \ . \tag{4.1}$$

179 In Eq. 4.1, $k = 2\pi/\lambda$ where λ is the wavelength of the isotopic time series. In Fig. 4.1 we illustrate the

180 effect of the diffusion transfer function on a range of wavelengths for $\sigma = 1, 2, 4$ and 8 cm. Wavelengths

181 on the order of 50 cm and above remain largely unaltered while signals with wavelengths shorter than

182 20 cm are heavily attenuated.

183   An estimate of the diffusion length σ can be obtained by looking at the power spectrum of the diffused

184 isotopic time series. Assuming a total noise signal $\eta(k)$ apparent in the time series, a model describing

185 the power spectrum is given by:

$$P_s = P_0(k)e^{-k^2\sigma^2} + |\hat{\eta}(k)|^2. \tag{4.2}$$

186 $P_0(k)$ is the spectral density of the compressed profile without diffusion. It is assumed independent

187 of k (now P_0) due to the strong depositional noise encountered in high resolution δ ice core series

188 (Johnsen et al. 2000). Moreover, Gkinis et al. (2014) showed that the redness of the climate signal does

189 not significantly affect the estimated diffusion lengths. The noise signal is generally described well by

190 autoregression of order 1 (AR-1), and its power spectral density is defined as (Kay & Marple 1981):

$$|\hat{\eta}(k)|^2 = \frac{\sigma_\eta^2 \Delta}{|1 - a_1 \exp(-ik\Delta)|^2}, \tag{4.3}$$

191 where a_1 is the AR-1 coefficient, σ_η^2 is the variance of the noise signal and Δ is the sample size. The

192 noise model combines the post depositional and measurement induced noise.

193   In Fig. 4.2, an example of power spectra based on a synthetic time series is shown. A description of

194 how the synthetic time series is generated is provided in Appendix D. This time series have been applied a

195 diffusion length of 8.40 cm. The spectral estimate of the time series $\mathbb{P}_s$ is calculated using Burg's spectral

196 estimation method (Kay & Marple 1981) and specifically the algorithm presented in Andersen (1974).

197 Using a least–squares approach we optimize the fit of the model P_s to the data series $\mathbb{P}_s$ by varying

the four parameters P_0, σ, a_1 and σ_η^2. In the case of Fig. 4.2, the $|P_s - \mathbb{P}_s|^2$ least squares optimization resulted in $P_0 = 0.35\,\%_0{}^2 \cdot \mathrm{m}$, $\sigma = 8.45\,\mathrm{cm}$, $a_1 = 0.05$ and $\sigma_\eta^2 = 0.005\,\%_0{}^2$.

Assuming a diffusion length $\widehat{\sigma}_i^2$ is obtained for depth z_i by means of $|P_s - \mathbb{P}_s|^2$ minimization, one can calculate the equivalent diffusion length at the bottom of the firn column σ_{firn}^2 in order to estimate firn temperatures by means of Eq. 2.7. In order to do this, one needs to take into account three necessary corrections - (1) sampling diffusion, (2) ice diffusion and (3) thinning. The first concerns the artifactually imposed diffusion due to the sampling of the ice core. In the case of a discrete sampling scheme with resolution Δ the additional diffusion length is (see Appendix E):

$$\sigma_{\mathrm{dis}}^2 = \frac{2\Delta^2}{\pi^2} \ln\left(\frac{\pi}{2}\right). \tag{4.4}$$

In the case of high resolution measurements carried out with CFA measurement systems, there exist a number of ways to characterize the sampling diffusion length. Typically the step or impulse response of the CFA system can be measured yielding a Gaussian filter specific for the CFA system (Gkinis et al. 2011, Emanuelsson et al. 2015, Jones et al. 2017). The Gaussian filter can be characterized by a diffusion length σ_{cfa}^2 that can be directly used to perform a sampling correction. The second correction concerns the ice diffusion as described in Sec. 3. The quantities σ_{ice}^2 and σ_{dis}^2 can be subtracted from $\widehat{\sigma}_i^2$ yielding a scaled value of σ_{firn}^2 due to ice flow thinning. As a result, we can finally obtain σ_{firn}^2 as:

$$\sigma_{\mathrm{firn}}^2 = \frac{\widehat{\sigma}_i^2 - \sigma_{\mathrm{dis}}^2 - \sigma_{\mathrm{ice}}^2}{\mathcal{S}(z)^2}. \tag{4.5}$$

The σ_{firn}^2 estimate is the cumulated diffusion that the signal has experienced. It is therefore only possible to obtain the integrated firn column temperature. This is done by calculating the root of the equation (for a known $A(z)$):

$$\left(\frac{\rho_{co}}{\rho_i}\right)^2 \sigma^2(\rho = \rho_{\mathrm{co}}, T(z), A(z)) - \sigma_{\mathrm{firn}}^2 = 0 \tag{4.6}$$

where σ^2 is the result of the integration in Eq. 2.7 from surface to close–off density ($\rho_o \to \rho_{\mathrm{co}}$). In this work we use a Newton-Raphson numerical scheme (Press et al. 2007) for the calculation of the roots of the equation.

While reconstructing temperatures, each input parameter to Eq. 4.6 (A, ρ_{co}, ρ_o, surface pressure P, $\mathcal{S}$ and σ_{ice}) is drawn from a Gaussian distribution with a predefined uncertainty (Table 4.1). This resembles uncertainties in the densification process, diffusion quantities and their parameterizations and inaccuracies in the ice flow thinning model. Moreover, this facilitates a better comparison between the single and differential diffusion techniques (Sec. 4.2) if one of the reconstruction methods is more sensitive to such uncertainties. The uncertainties might be lower for a specific ice core as an input parameter e.g. A can

225 be well constrained from other climate proxies. This would decrease the uncertainty and hereby increase
226 the precision of the temperature reconstructions.

Table 4.1: The standard deviations of the input parameters. Most of the standard deviations are expressed as a percentage of the mean input value.

Parameter	A	ρ_{co}	ρ_o	P	$\mathcal{S}$	σ_{ice}
Uncertainty	$\pm 5\% A_{\mathrm{mean}}$	$\pm 20\,\mathrm{kg m^{-3}}$	$\pm 30\,\mathrm{kg m^{-3}}$	$\pm 2\% P_{\mathrm{mean}}$	$\pm 1\% \mathcal{S}_{\mathrm{mean}}$	$\pm 2\% \sigma_{ice_{\mathrm{mean}}}$

227 The accuracy of the σ_{firn}^2 estimation and subsequently of the temperature reconstruction obtained based
228 on it, depends on the three correction terms σ_{ice}^2, σ_{dis}^2 and the ice flow thinning $\mathcal{S}(z)$. For relatively
229 shallow depths where σ_{ice}^2 is relatively small compared to $\widehat{\sigma}_i^2$, ice diffusion can be accounted for with
230 simple assumptions on the borehole temperature profile and the ice flow. In a similar way, σ_{dis}^2 is a well
231 constrained parameter and depends only on the sampling resolution Δ for discrete sampling schemes or
232 the smoothing of the CFA measurement system.

233 Equation 4.5 reveals an interesting property of the single isotopologue temperature estimation technique.
234 As seen, the result of the σ_{firn}^2 calculation depends strongly on the ice flow thinning quantity $\mathcal{S}(z)^2$.
235 Possible errors in the estimation of $\mathcal{S}(z)^2$ due to imperfections in the modelling of the ice flow will
236 inevitably be propagated to the σ_{firn}^2 value thus biasing the temperature estimation. Even though this
237 appears to be a disadvantage in the method, in some instances, it can be a useful tool for assessing the
238 accuracy of ice flow models. Provided that for certain sections of the ice core there is a temperature
239 estimate available based on other reconstruction methods (borehole thermometry, $\delta^{15}\mathrm{N}$/ $\delta^{40}\mathrm{Ar}$) it is
240 possible to estimate ice flow induced thinning of the ice core layers. Following this approach Gkinis
241 et al. (2014) proposed a correction in the existing accumulation rate history for the NorthGRIP ice core.

242 *The annual spectral signal interference*

243 For some of the processed ice core data, we observed a prominent spectral feature at the low frequency
244 area coinciding with the annual water isotopic signal (i.e. an annual peak in the spectum). The annual
245 peak is prominent in ice cores with boundary conditions that mitigate the effects of firn diffusion, notably
246 low temperatures and high accumulation rates. The resulting effect of such a spectral signature, is the
247 artifactual biasing of the diffusion length estimation towards lower values and thus colder temperatures.
248 Figure 4.3 shows the PSD of the δD series for a mid Holocene section from the GRIP ice core (drill site
249 characteristics in Table 5.2). A prominent spectral feature is visible at $f \approx 6\,\mathrm{cycles\,m^{-1}}$. This frequency
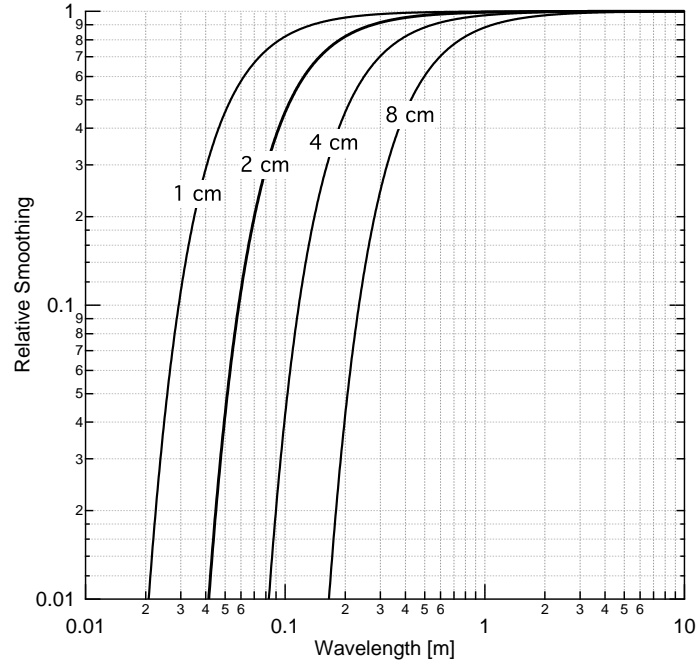
Figure 4.1: The smoothing effect of the diffusion transfer function demonstrated on a range of different wavelengths for $\sigma = 1$, 2, 4 and 8 cm.

is comparable to the expected frequency of the annual signal at $6.1 \, \mathrm{cycles \, m^{-1}}$ as estimated from the annual layer thickness reconstruction of the GICC05 timescale (Vinther et al. 2006).

In order to evade the influence of the annual spectral signal on the diffusion length estimation, we propose the use of a weight function $w(f)$ in the spectrum as:

$$w(f) = \begin{cases} 0 & f_\lambda - \mathrm{d}f_\lambda \leq f \leq f_\lambda + \mathrm{d}f_\lambda \\ 1 & f < f_\lambda - \mathrm{d}f_\lambda, f > f_\lambda + \mathrm{d}f_\lambda \end{cases} \tag{4.7}$$

where f_λ is the frequency of the annual layer signal based on the reconstructed annual layer thickness λ and $\mathrm{d}f_\lambda$ is the range around the frequency f_λ at which the annual signal is detectable. The weight function is multiplied with the optimization norm $|P_s - \mathbb{P}_s|^2$. Figure 4.3 also illustrates the effect of the weight function on the estimation of P_s and subsequently the diffusion length value. When the weight function is used during the optimization process, there is an increase in the diffusion length value by 0.2 cm, owing essentially to the exclusion of the annual signal peak from the minimization of $|P_s - \mathbb{P}_s|^2$. While the value of f_λ can be roughly predicted, the value of $\mathrm{d}f_\lambda$ usually requires visual inspection of the spectrum.
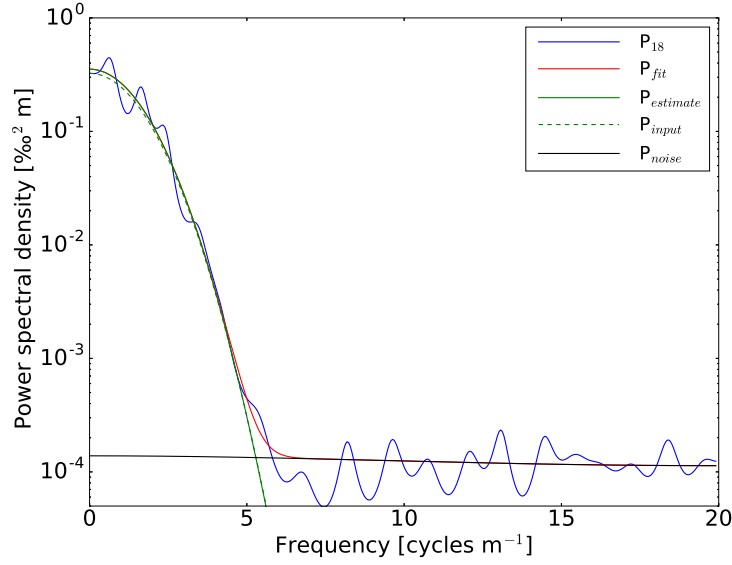
Figure 4.2: PSD of a synthetic δ^{18}O time series plotted with respect to frequency (blue curve). The red curve represents the complete model fit (Eq. 4.2). The green dashed curve represents the input diffusion and the the solid green curve represents the estimated diffusion length of the signal. The black curve represents the noise part of the fit.

Appendix F shows the fitted PSD of all the ice core time series introduced in Sec. 5.2. Annual peak corrections are implemented in three out of thirteen ice core data series (GRIP late and mid Holocene and NEEM late Holocene). For a specific ice core section's f_λ, the chosen weight function is in all three cases $w(f_\lambda - 0.5 \leq f \leq f_\lambda + 3) = 0$.

No distinguished multiannual variability exists in any of the ice core spectra as seen in Appendix F. A correction is therefore not implemented despite that climatic modes such as the North Atlantic Oscillation, El Niño-Southern Oscillation/Pacific Decadal Oscillation and the Southern Annular Mode have the potential to artifactually affect the diffusion length estimate in a similar way as the annual peak.

4.2 The differential diffusion signal

A second-order temperature reconstruction technique is possible based on the differential signal between δ^{18}O and δD. Due to the difference in the fractionation factors and the air diffusivities between the oxygen and deuterium isotopologues, a differential diffusion signal is created in the firn column. Based on the calculation of the diffusion lengths presented in Fig. 2.1 we then compute the differential diffusion lengths
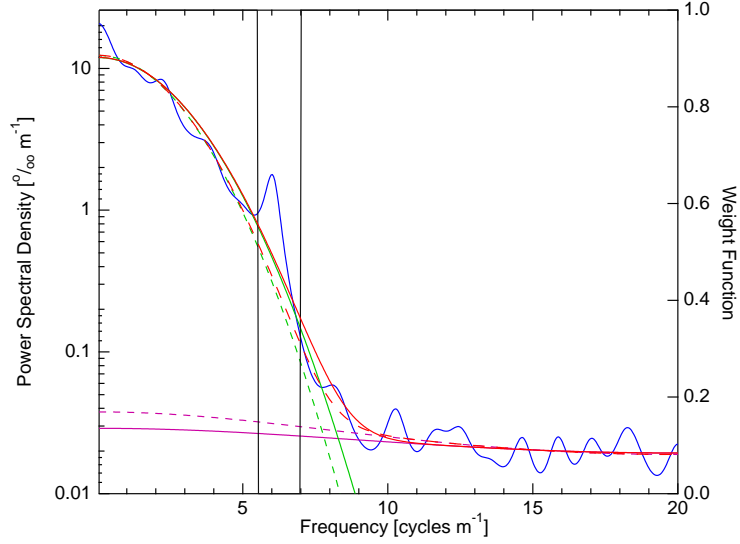
Figure 4.3: The interference of the annual spectral signal is seen in the PSD of the δD GRIP mid Holocene section. The regular fit is represented by the solid lines and the dashed lines represent the case where the weight function $w(f)$ has filtered out this artifactual bias.

$^{17}\Delta\sigma^2$ and $^{18}\Delta\sigma^2$ where

$$^{17}\Delta\sigma^2 = \sigma_{17}^2 - \sigma_{\mathrm{D}}^2 \;\text{ and }\; ^{18}\Delta\sigma^2 = \sigma_{18}^2 - \sigma_{\mathrm{D}}^2. \tag{4.8}$$

As it can be seen in Fig. 4.4 the differential diffusion length signal is slightly larger for the case of $^{17}\Delta\sigma^2$ when compared to $^{18}\Delta\sigma^2$.

One obvious complication of the differential diffusion technique is the requirement for dual measurements of the water isotopologues, preferably performed on the same sample. The evolution of IRMS techniques targeting the analysis of δD (Bigeleisen et al. 1952, Vaughn et al. 1998, Gehre et al. 1996, Begley & Scrimgeour 1997) in ice cores has allowed for dual isotopic records at high resolutions. With the advent of CRDS techniques and their customisation for CFA measurements, simultaneous high resolution measurements of both δ^{18}O and δD have become a routine procedure.

The case of δ^{17}O is more complicated as the greater abundance of ^{13}C than ^{17}O rules out the possibility for an IRMS measurement at mass/charge ratio (m/z) of 45 or 29 using CO_2 equilibration or reduction to CO respectively. Alternative approaches that exist include the electrolysis method with $CuSO_4$ developed by Meijer & Li (1998) as well as the fluorination method presented by Baker et al. (2002) and implemented by Barkan & Luz (2005) for dual-inlet IRMS systems. These techniques target the measurement of the

289 $^{17}O_{excess}$ parameter and are inferior for $\delta^{17}O$ measurements at high precision and have a very low sample

290 throughput. As a result, high resolution $\delta^{17}O$ measurements from ice cores are currently non existent.

291 Recent innovations however in CRDS spectroscopy (Steig et al. 2014) allow for simultaneous triple

292 isotopic measurements of δD, $\delta^{18}O$ and $\delta^{17}O$ in a way that a precise and accurate measurement for both

293 $\delta^{17}O$ and $^{17}O_{excess}$ is possible. Therefore high resolution ice core datasets of δD, $\delta^{18}O$ and $\delta^{17}O$ should

294 be expected in the near future.

295   The following analysis is focused on the $^{18}\Delta\sigma^2$ signal but it applies equally to the $^{17}\Delta\sigma^2$. The stronger

296 attenuation of the $\delta^{18}O$ signal with respect to the δD signal can be visually observed in the power spectral

297 densities of the two signals. As seen in Fig. 4.5 the $\mathbb{P}_{S18}$ signal reaches the noise level at a lower frequency

298 when compared to the $\mathbb{P}_{SD}$ signal. At low frequencies with high signal to noise ratio we can calculate

299 the logarithm of the ratio of the two power spectral densities as (i.e. neglecting the noise term):

$$\ln\left(\frac{P_D}{P_{18}}\right) \approx k^2 \left(\sigma_{18}^2 - \sigma_D^2\right) + \ln\left(\frac{P_{0_D}}{P_{0_{18}}}\right) = {}^{18}\Delta\sigma^2 \, k^2 + C. \tag{4.9}$$

300 As seen in Eq. 4.9 and Fig. 4.5 (synthetic generated $\delta^{18}O$ and δD data as in Sec. 4.1) an estimate

301 of the $^{18}\Delta\sigma^2$ parameter can be obtained by a linear fit of $\ln\left(P_D/P_{18}\right)$ in the low frequency area,

302 thus requiring only two parameters $\left({}^{18}\Delta\sigma^2 \, \text{and} \, C\right)$ to be tuned. An interesting aspect of the differential

303 diffusion method, is that in contrast to the single isotopologue diffusion length, $^{18}\Delta\sigma_{firn}^2$ is a quantity

304 that is independent of the sampling and solid ice diffusion thus eliminating the uncertainties associated

305 with these two parameters. This can be seen by simply using Eq. 4.5:

$$^{18}\Delta\sigma_{firn}^2 = \frac{\hat{\sigma}_{18}^2 - \sigma_{dis}^2 - \sigma_{ice}^2}{\mathcal{S}(z)^2} - \frac{\hat{\sigma}_D^2 - \sigma_{dis}^2 - \sigma_{ice}^2}{\mathcal{S}(z)^2} = \frac{\hat{\sigma}_{18}^2 - \hat{\sigma}_D^2}{\mathcal{S}(z)^2}. \tag{4.10}$$

306 Accurate estimates of the thinning function however still play a key role in the differential diffusion

307 technique. One more complication of the differential diffusion technique is the selection of the frequency

308 range in which one chooses to apply the linear regression. Often visual inspection is required in order to

309 designate a cut-off frequency until which the linear regression can be applied. In most cases identifying

310 the cut-off frequency, or at least a reasonable area around it is reasonably straight-forward. Though in a

311 small number of cases, spectral features in the low frequency area seem to have a strong influence on

312 the slope of the linear regression and thus on the $^{18}\Delta\sigma^2$. As a result, visual inspection of the regression

313 result is always advised in order to avoid biases.

314   Another way of estimating the differential diffusion signal is to subtract the single diffusion spectral

315 estimates σ_{18}^2 and σ_D^2. Theoretically this approach should be inferior to the linear fit approach due to

316 the fact that more degrees of freedom are involved in the estimation of σ_{18}^2 and σ_D^2 (8 versus 2; 3 if the

317 cutoff frequency is included). Here we will test both approaches.

Linear correlation method

An alternative way to calculate the differential diffusion signal $^{18}\Delta\sigma^2$ is based on the assumption that the initial precipitated isotopic signal presents a d_{xs} that is invariable with time and as a consequence of this, the correlation signal between $\delta^{18}O$ and δD (hereafter $r_{\delta^{18}O/\delta D}$) is expected to have a maximum value at the time of deposition. The d_{xs} signal is defined as the deviation from the metoric water line $d_{xs} = \delta D - 8 \cdot \delta^{18}O$ (Craig 1961, Dansgaard 1964). From the moment of deposition, the difference in diffusion between the $\delta^{18}O$ and δD signals results in a decrease of the $r_{\delta^{18}O/\delta D}$ value. Hence, diffusing the δD signal with a Gaussian kernel of standard deviation equal to $^{18}\Delta\sigma^2$ will maximize the value of $r_{\delta^{18}O/\delta D}$ (van der Wel et al. 2015) as shown in Fig. 4.6. Thus, the $^{18}\Delta\sigma^2$ value is found when the $r_{\delta^{18}O/\delta D}$ value has its maximum.

This type of estimation is independent of spectral estimates of the $\delta^{18}O$ and δD time series and does not pose any requirements for measurement noise characterization or selection of cut-off frequencies. However uncertainties related to the densification and ice flow processes, affect this method equally as they do for the spectrally based differential diffusion temperature estimation. In this study, we test the applicability of the method on synthetic and real ice core data. We acknowledge that the assumption that the d_{xs} signal is constant with time is not entirely consistent with the fact that there is a small seasonal cycle in the d_{xs} signal (Johnsen & White 1989). It is thus likely to result in inaccuracies.

4.3 The diffusion length ratio

A third way of using the diffusion lengths as proxies for temperature can be based on the calculation of the ratio of two different diffusion lengths. From Eq. 2.7 we can evaluate the ratio of two different isotopologues j and k as:

$$\frac{\sigma_j^2(\rho)}{\sigma_k^2(\rho)} = \frac{\dfrac{1}{\rho^2}\int 2\rho^2\left(\dfrac{d\rho}{dt}\right)^{-1}D_j(\rho)\,d\rho}{\dfrac{1}{\rho^2}\int 2\rho^2\left(\dfrac{d\rho}{dt}\right)^{-1}D_k(\rho)\,d\rho}, \tag{4.11}$$

and by substituting the firn diffusivities as defined in Appendix A and according to Johnsen et al. (2000) we get:

$$\frac{\sigma_j^2(\rho)}{\sigma_k^2(\rho)} = \frac{D_{aj}\alpha_k}{D_{ak}\alpha_j}\frac{\dfrac{1}{\rho^2}\int 2\rho^2\left(\dfrac{d\rho}{dt}\right)^{-1}\dfrac{m\,p}{R\,T\,\tau}\left(\dfrac{1}{\rho}-\dfrac{1}{\rho_{ice}}\right)d\rho}{\dfrac{1}{\rho^2}\int 2\rho^2\left(\dfrac{d\rho}{dt}\right)^{-1}\dfrac{m\,p}{R\,T\,\tau}\left(\dfrac{1}{\rho}-\dfrac{1}{\rho_{ice}}\right)d\rho} = \frac{D_{aj}\alpha_k}{D_{ak}\alpha_j}. \tag{4.12}$$

As a result, the ratio of the diffusion lengths is dependent on temperature through the parameterizations of the fractionation factors (α) and carries no dependence to parameters related to the densification rates nor the atmospheric pressure. Additionally, it is a quantity that is independent of depth. Here we give
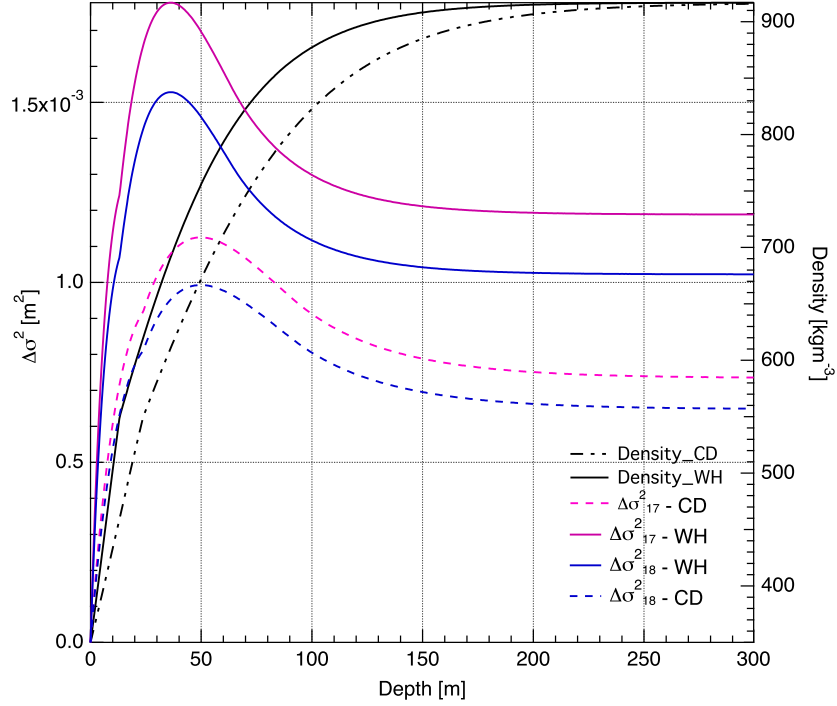
Figure 4.4: Differential diffusion length profiles for cases A (solid lines) and B (dashed lines) for $^{18}\Delta\sigma^2$ (blue) and $^{17}\Delta\sigma^2$ (purple). The density profiles are given in black.

the analytical expressions of all the isotopologues combinations by substituting the diffusivities and the fractionation factors:

$$\sigma_{18}^2/\sigma_{\mathrm{D}}^2 = 0.93274 \cdot \exp(16288/T^2 - 11.839/T) \tag{4.13}$$

$$\sigma_{17}^2/\sigma_{\mathrm{D}}^2 = 0.933 \cdot \exp(16288/T^2 - 6.263/T) \tag{4.14}$$

$$\sigma_{18}^2/\sigma_{17}^2 = 0.99974 \cdot \exp(-5.57617/T) \tag{4.15}$$

A data-based diffusion length ratio estimate can be obtained by estimating the single diffusion length values as described in Sec. 4.1 and thereafter applying the necessary corrections as in Eq. 4.5. An interesting aspect of the ratio estimation is that it is not dependent on the ice flow thinning as seen below

$$\left(\frac{\sigma_{18}^2}{\sigma_{\mathrm{D}}^2}\right)_{\mathrm{firn}} = \frac{\hat{\sigma}_{18}^2 - \sigma_{\mathrm{dis}}^2 - \sigma_{\mathrm{ice}}^2}{\hat{\sigma}_{\mathrm{D}}^2 - \sigma_{\mathrm{dis}}^2 - \sigma_{\mathrm{ice}}^2}. \tag{4.16}$$

while the method still depends on the sampling and ice diffusion.
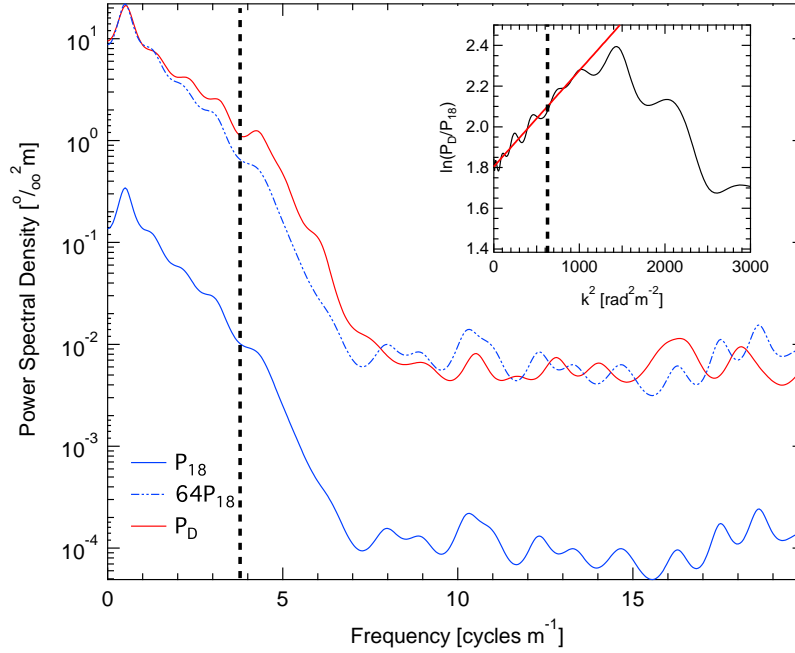
Figure 4.5: PSDs of synthetic δ^{18}O (blue) and δD (red) with respect to frequency where the inner subplot shows the $\ln\left(P_{\mathrm{D}}/P_{18}\right)$ relation with respect to k^2. The $^{18}\Delta\sigma^2$ value is determined from the slope of the linear fit in the subplot. The chosen cutoff frequency is marked by the vertical dashed line in both plots.

5 RESULTS

5.1 Synthetic data test

We present here a test of accuracy and precision for the estimates of the various quantities used for diffusion based temperature estimations outlined in Sec. 4. The tests consist of the generation of synthetic data for δ^{17}O, δ^{18}O and δD and subsequent numerical diffusion with diffusion lengths as calculated for case A and B (as presented in Fig. 2.1). The time series are then sampled at a resolution of $2.5\,\mathrm{cm}$ and white measurement noise is added. Eventually, estimates of diffusion lengths for all three isotopologues are obtained using the techniques we have described in the previous sections. The full description of how the synthetic data are generated is outlined in Appendix D.

The process of time series generation is repeated 500 times. For each iteration, the quantities σ_{17}, σ_{18}, σ_{D}, $^{17}\Delta\sigma^2$, $^{18}\Delta\sigma^2$ and the ratios $\sigma_{18}^2/\sigma_{\mathrm{D}}^2$, $\sigma_{17}^2/\sigma_{\mathrm{D}}^2$ and $\sigma_{18}^2/\sigma_{17}^2$ are estimated. The differential diffusion signals are estimated using the three different techniques as described in Sec. 4.2. We designate the subtraction technique with I, the linear regression with II and the correlation method with III. For every
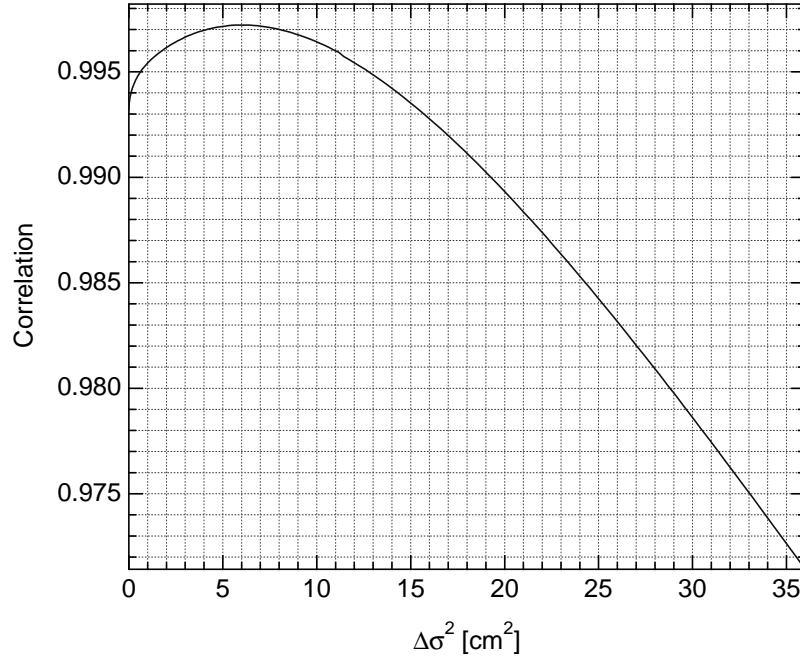
Figure 4.6: Correlation coefficient ($r_{\delta^{18}O/\delta D}$) between the $\delta^{18}O$ and the forward–diffused δD series as a function of the estimated $^{18}\Delta\sigma^2$. The synthetic data represent a case A climate.

363 value of the diffusion estimates we calculate a firn temperature where the uncertainties related to the firn

364 diffusion model (A, ρ_{co}, ρ_o, P, $\mathcal{S}$ and σ_{ice} in Table 4.1) are included. Finally for the total of the 500

365 iterations we calculate a mean firn temperature $\overline{T}$, a standard deviation and a mean bias as:

$$\text{MB} = \frac{1}{N}\sum_{i=1}^{N} T_i - T_{\text{sur}} = \overline{T} - T_{\text{sur}}, \tag{5.1}$$

366 where $i = 1, 2, \ldots, N$ signifies the iteration number, T_i is the synthetic data-based estimated temperature

367 and T_{sur} is the model forcing surface temperature for the case A and B scenarios. For each technique, the

368 precision $s_{\overline{T}}$ is calculated by averaging the squared standard deviations of all simulations. The results of

369 the experiment are presented in Table 5.1 and the calculated mean biases are illustrated in Fig. 5.1. The

370 diffusion length ratio approach yields very large uncertainty bars (see Table 5.1) and thus these results

371 are not included in Fig. 5.1.

372 *5.2 Ice core data test*

373   We also use a number of high resolution, high precision ice core data, in order to benchmark the

374 diffusion temperature reconstruction techniques that we have presented. The aim of this benchmark test
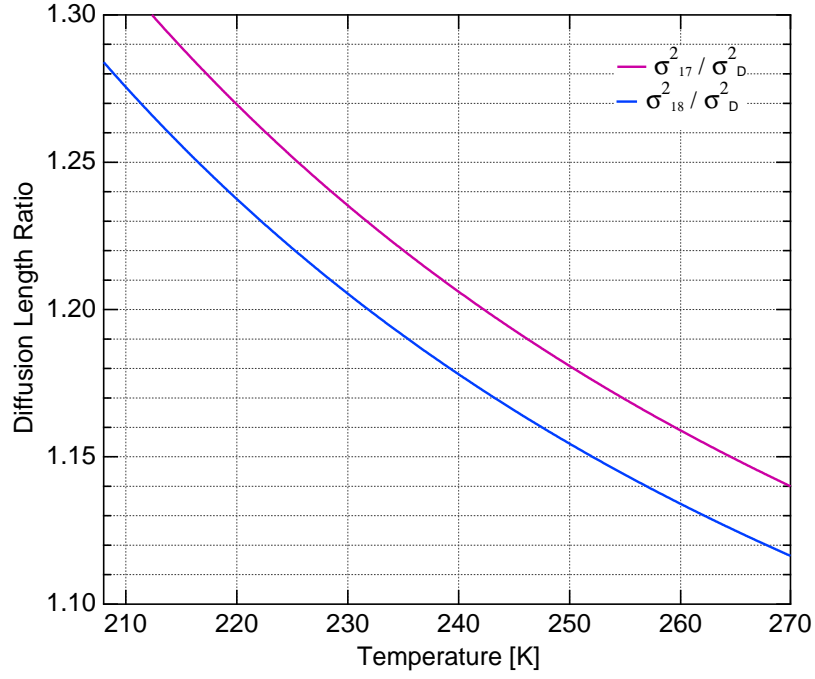
Figure 4.7: The diffusion length ratios σ_{18}^2/σ_D^2 and σ_{17}^2/σ_D^2 with respect to temperature. The $\sigma_{18}^2/\sigma_{17}^2$ is almost constant at 0.975 and omitted here due to its very low temperature sensitivity.
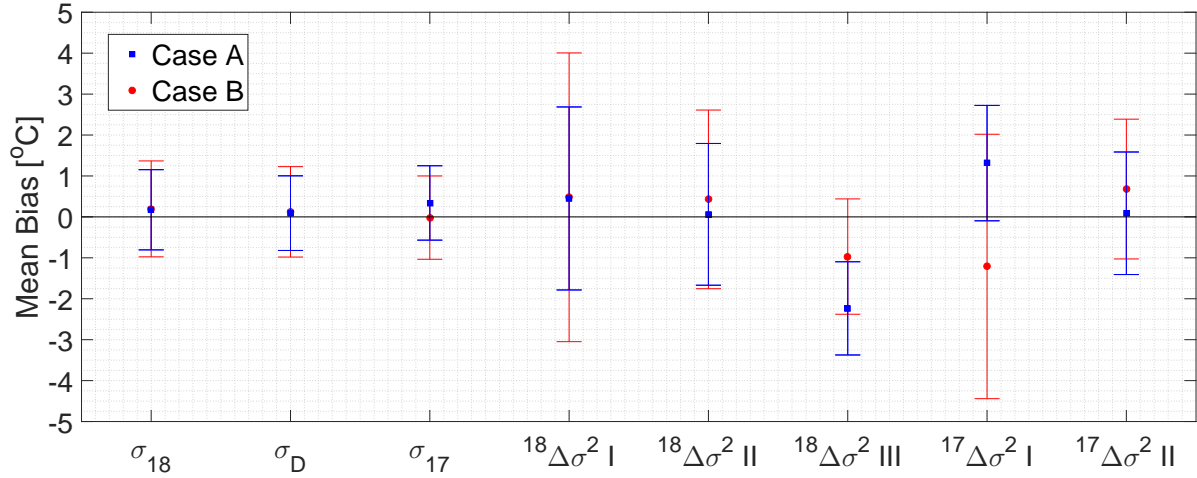

Figure 5.1: Mean biases for the single and differential diffusion techniques. The error bars represent 1 std of the estimated temperatures.

	Case A			Case B		
	Applied diffusion	Est. diffusion	Est. T [^{o}C]	Applied diffusion	Est. diffusion	Est. T [^{o}C]
σ_{18}	5.82 cm	5.85 ± 0.14 cm	-54.8 ± 1.0	8.50 cm	8.51 ± 0.20 cm	-28.8 ± 1.2
σ_{D}	5.22 cm	5.23 ± 0.12 cm	-54.9 ± 0.9	7.86 cm	7.86 ± 0.18 cm	-28.9 ± 1.1
σ_{17}	5.90 cm	5.97 ± 0.11 cm	-54.7 ± 0.9	8.59 cm	8.54 ± 0.13 cm	-29.0 ± 1.0
$^{18}\Delta\sigma^2$ I	6.6 cm^2	6.9 ± 1.1 cm^2	-54.6 ± 2.2	10.3 cm^2	10.7 ± 2.0 cm^2	-28.5 ± 3.5
$^{18}\Delta\sigma^2$ II	6.6 cm^2	6.7 ± 0.8 cm^2	-54.9 ± 1.7	10.3 cm^2	10.5 ± 1.2 cm^2	-28.6 ± 2.2
$^{18}\Delta\sigma^2$ III	6.6 cm^2	5.5 ± 0.3 cm^2	-57.2 ± 1.1	10.3 cm^2	9.7 ± 0.6 cm^2	-30.0 ± 1.4
$^{17}\Delta\sigma^2$ I	7.5 cm^2	8.3 ± 0.7 cm^2	-53.7 ± 1.4	12.0 cm^2	12.2 ± 2.0 cm^2	-30.2 ± 3.2
$^{17}\Delta\sigma^2$ II	7.5 cm^2	7.5 ± 0.5 cm^2	-54.9 ± 1.5	12.0 cm^2	12.4 ± 1.0 cm^2	-28.3 ± 1.7
$\sigma_{18}^2/\sigma_{17}^2$	0.975	0.960 ± 0.027	————	0.977*	0.993 ± 0.035*	————
$\sigma_{18}^2/\sigma_{\mathrm{D}}^2$	1.24	1.25 ± 0.04	-56.6 ± 11.1	1.17	1.17 ± 0.03	-28.2 ± 19.3
$\sigma_{17}^2/\sigma_{\mathrm{D}}^2$	1.28	1.31 ± 0.03	-62.8 ± 7.0	1.20	1.18 ± 0.04	-16.1 ± 27

Table 5.1: Simulations with synthetic data of a case A ($T_{\mathrm{sur}} = -55.0\,^{o}$C) and B ($T_{\mathrm{sur}} = -29.0\,^{o}$C). The diffusion lengths in the tabular are the firn diffusion lengths. Thus, this is before sampling, ice diffusion and thinning affected the input diffusion length. The estimated firn diffusion lengths are after correcting for sampling, ice diffusion and thinning (with their corresponding uncertainties).

is to utilize the various reconstruction techniques for a range of boundary conditions that is (a) as broad as possible with respect to mean annual surface temperature and accumulation and (b) representative of existing polar ice core sites. Additionally, we have made an effort in focusing on ice core data sets that reflect conditions as close as possible to present. As a result, the majority of the data sets presented here are from relatively shallow depths and as a result reflect climatic conditions typical of the late Holocene. Where this was not possible due to limited data availability, we have used data originating from deeper sections of the ice cores with an age of about 10ka b2k reflecting conditions of the early Holocene. In Table 5.2 we provide relevant information for each data set as well as the present temperature and accumulation conditions for the drill site from which each data set originates.

The data sets were produced using a variety of techniques both with respect to the analysis itself (IRMS/CRDS), as well as with respect to the sample resolution and preparation (discrete/CFA). The majority of the data sets were analysed using CRDS instrumentation. In particular the L1102i, L2120i and L2130i variants of the Picarro CRDS analyser were utilized for both discrete and CFA measurements of δ^{18}O and δD. The rest of the data sets were analysed using IRMS techniques with either CO_2 equilibration or high temperature carbon reduction. For the case of the NEEM early Holocene data set, we work with

390   two data sections that span the same depth interval and consist of discretely sampled and CFA measured

391   data respectively. Additionally, the Dome C and Dome F data sections represent conditions typical for

392   the East Antarctic Plateau and are sampled using a different approach (2.5 cm resolution discrete samples

393   for the Dome C section and high resolution CFA measurements for the Dome F section).

394   In a way similar to the synthetic data test, we apply the various reconstruction techniques on every ice

395   core data section, we estimate the corresponding diffusion parameters and subsequently the temperatures

396   corresponding to them. No reconstruction techniques involving $\delta^{17}O$ are presented here due to lack of

397   $\delta^{17}O$ data. In order to achieve an uncertainty estimation for every reconstruction, we perform a sensitivity

398   test that is based on 1000 repetitions. Assuming that every ice core section consists of J $\delta^{18}O$ and

399   δD points, then a repetition is based on a data subsection with size J' that varies in the interval $[J/2, J]$.

400   This "jittering" of the subsection size happens around the midpoint of every section and J' is drawn from

401   a uniform distribution. Eventually, for every reconstruction method and every ice core site, we calculate

402   a mean and a standard deviation for the diffusion estimate, as well as a mean and a standard deviation

403   for the temperature. The standard deviation accounts for uncertainties related to both the estimation of

404   the diffusion length and uncertainties originating from the firn diffusion model, ice flow thinning model

405   and ice diffusion (through the parameters: A, ρ_{co}, ρ_o, P, $\mathcal{S}$ and σ_{ice}). Results are presented in Table 5.3.

406   The estimated temperatures for ice cores covering the late-mid Holocene and early Holocene are shown

407   in Fig. 5.2 and 5.3 respectively.

408 *5.3 The fractionation factors*

409   The influence of the fractionation factors (α_{18}, α_D) on the reconstructed temperatures are tested

410   on ice core data sets representative of a broad range of temperatures. By comparing the results of

411   different parameterization schemes, it is possible to quantify the influence of the choice of parametrization

412   on the absolute temperature estimates. This is especially relevant for temperatures below $-40^{\circ}C$, as

413   the confidence of the parameterized fractionation factors have been shown to be low for such cold

414   temperatures (Ellehoj et al. 2013). Similar to the ice core data test (Sec. 5.2), the corresponding diffusion

415   parameters and subsequently the temperatures are based on a sensitivity test of 1000 repetitions. The

416   results are displayed in Fig. 5.4, where the temperatures resulting from the parametrizations of Majoube

417   (1970) (α_{18}) and Merlivat & Nief (1967) (α_D) are compared to the temperatures resulting from the

418   parametrizations of Ellehoj et al. (2013) (α_{18}, α_D) and Lamb et al. (2017) (α_D). In the latter case, the

419   parameterization of α_{18} from Majoube (1970) is used for the dual diffusion length methods.

Table 5.2: Ice core data sections and the corresponding drill site characteristic. Sources of data: (Steig et al. 2013)[1], (Oerter et al. 2004)[2], (Svensson et al. 2015)[3], (Gkinis 2011)[4], (Gkinis et al. 2011)[5]. Drill site characteristic sources: (Banta et al. 2008)[a], (Oerter et al. 2004, Veres et al. 2013)[b], (Watanabe et al. 2003, Kawamura et al. 2003)[c], (Lorius et al. 1979)[d], (NGRIP members 2004, Gkinis et al. 2014)[e], (Johnsen et al. 2000)[f], (Guillevic et al. 2013, Rasmussen et al. 2013)[g].

Site Name	Depth [m]	Age [kab2k]	Present T [°C]	A [m ice yr⁻¹]	P [Atm]	Thinning	Meas.	Analysis	Δ [cm]
GRIP mid[f]	753 − 776	3.7	−31.6	0.23	0.65	0.71	$\delta D, \delta^{18}O$	2130	2.5
GRIP late[f]	514 − 531	2.4	−31.6	0.23	0.65	0.79	$\delta D, \delta^{18}O$	2130	2.5
WAIS 2005A[a,1]	260 − 290	1.1	−31.1	0.22	0.77	0.92	$\delta^{18}O$	1102	5.0
EDML[b,2]	123 − 178	1.6	−44.6	0.08	0.67	0.93	$\delta D, \delta^{18}O$	IRMS	5.0
NEEM[g]	174 − 194	0.8	−29.0	0.22	0.72	0.31	$\delta D, \delta^{18}O$	2120	2.5
NGRIP[e]	174 − 194	0.9	−31.5	0.20	0.67	0.49	$\delta^{18}O$	IRMS	2.5
Dome F[c,3]	302 − 307	9.6	−57.3	0.04	0.61	0.93	$\delta D, \delta^{18}O$	CFA1102	0.5
Dome C[d,4]	308 − 318	9.9	−53.5	0.04	0.65	0.93	$\delta D, \delta^{18}O$	IRMS	2.5
GRIP early[f]	1449 − 1466	9.4	−31.6	0.23	0.65	0.42	$\delta D, \delta^{18}O$	2130	2.5
NEEM dis[g,5]	1380 − 1392	10.9	−29.0	0.22	0.72	0.31	$\delta D, \delta^{18}O$	2120	5.0
NEEM CFA[g,5]	1382 − 1399	10.9	−29.0	0.22	0.72	0.31	$\delta D, \delta^{18}O$	CFA1102	0.5
NGRIP I[e]	1300 − 1320	9.1	−31.5	0.18	0.67	0.55	$\delta^{18}O$	IRMS	5.0
NGRIP II[e]	1300 − 1320	9.1	−31.5	0.18	0.67	0.55	$\delta^{18}O$	IRMS	5.0
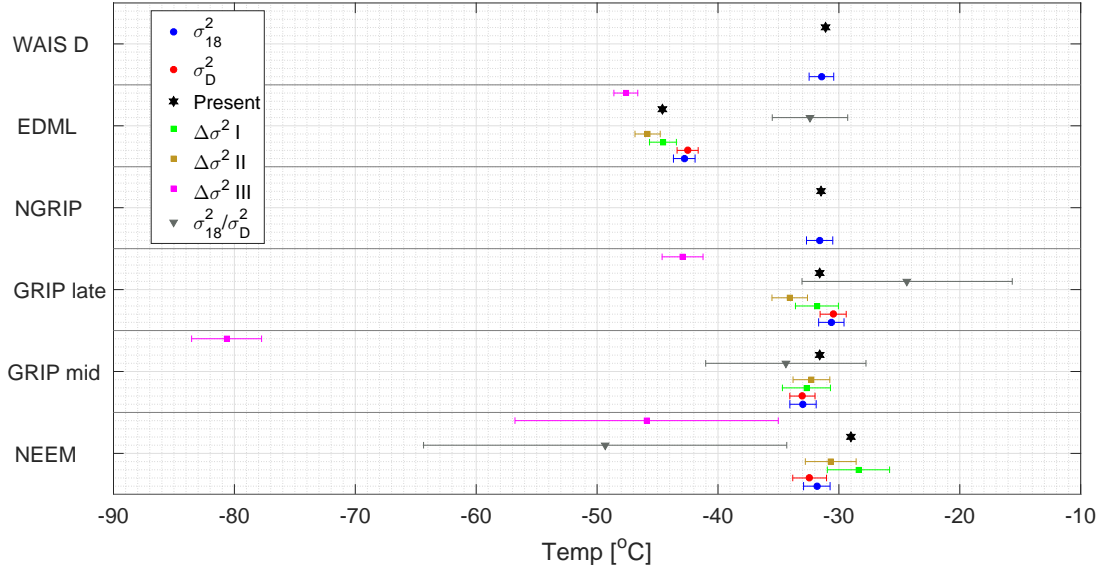
Figure 5.2: Late-mid Holocene section with reconstructed temperatures from the σ_{18}^2 (blue circles), σ_D^2 (red circles), $\Delta\sigma^2$ I (green squares), $\Delta\sigma^2$ II (brown squares), $\Delta\sigma^2$ III (magenta squares) and σ_{18}^2/σ_D^2 (grey triangles) methods. The black stars represent the present annual mean temperatures at the sites.
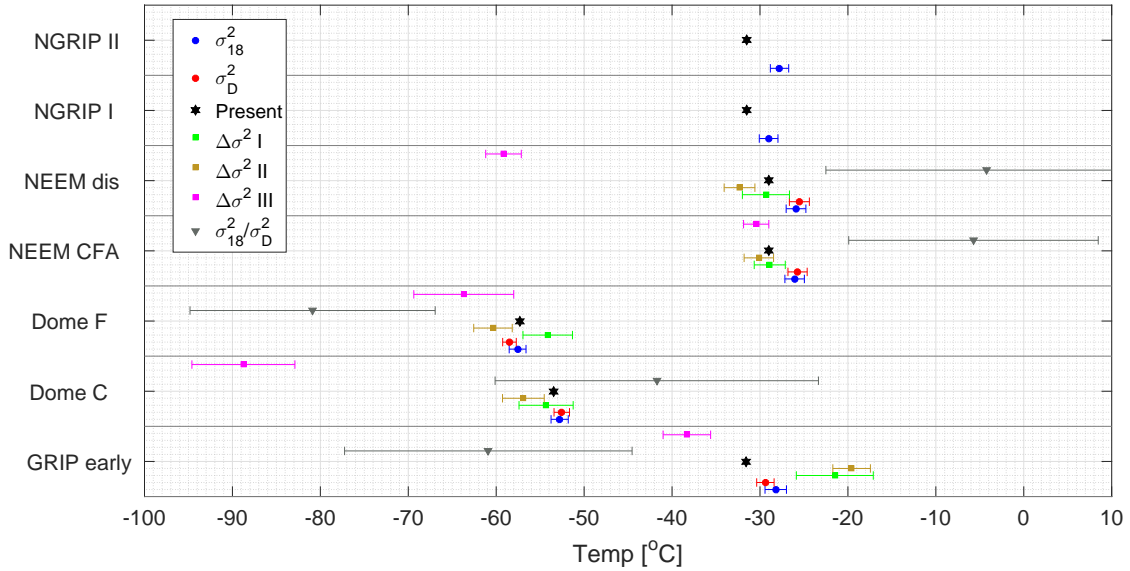

Figure 5.3: Early Holocene section with reconstructed temperatures from the σ_{18}^2 (blue circles), σ_D^2 (red circles), $\Delta\sigma^2$ I (green squares), $\Delta\sigma^2$ II (brown squares), $\Delta\sigma^2$ III (magenta squares) and σ_{18}^2/σ_D^2 (grey triangles) methods. The black stars represent the present annual mean temperatures at the sites.

Table 5.3: Ice core results with the estimated firn diffusion lengths and their corresponding temperatures [°C]. The units for the σ_{18} and the σ_{D} values are expressed in cm and the unit for $^{18}\Delta\sigma^2$ is expressed in cm^2.

Site Name	σ_{18}	σ_{D}	$^{18}\Delta\sigma^2$ I	$^{18}\Delta\sigma^2$ II	$^{18}\Delta\sigma^2$ III	$\sigma_{18}^2/\sigma_{\mathrm{D}}^2$
GRIP mid	$7.83 \pm 0.17\,\mathrm{cm}$	$7.20 \pm 0.16\,\mathrm{cm}$	$9.4 \pm 1.0\,\mathrm{cm}^2$	$9.6 \pm 0.7\,\mathrm{cm}^2$	$0.2 \pm 0.1\,\mathrm{cm}^2$	1.18 ± 0.02
	$-33.0 \pm 1.1\,°\mathrm{C}$	$-33.0 \pm 1.0\,°\mathrm{C}$	$-32.7 \pm 2.0\,°\mathrm{C}$	$-32.3 \pm 1.5\,°\mathrm{C}$	$-80.6 \pm 2.9\,°\mathrm{C}$	$-34.4 \pm 6.6\,°\mathrm{C}$
GRIP late	$8.52 \pm 0.12\,\mathrm{cm}$	$7.92 \pm 0.16\,\mathrm{cm}$	$9.9 \pm 0.8\,\mathrm{cm}^2$	$8.6 \pm 0.5\,\mathrm{cm}^2$	$4.8 \pm 0.5\,\mathrm{cm}^2$	1.16 ± 0.02
	$-30.6 \pm 1.1\,°\mathrm{C}$	$-30.5 \pm 1.1\,°\mathrm{C}$	$-31.8 \pm 1.8\,°\mathrm{C}$	$-34.1 \pm 1.5\,°\mathrm{C}$	$-43.0 \pm 1.7\,°\mathrm{C}$	$-24.4 \pm 8.7\,°\mathrm{C}$
WAIS 2005A	$6.95 \pm 0.15\,\mathrm{cm}$	————	————	————	————	————
	$-31.5 \pm 1.0\,°\mathrm{C}$	————	————	————	————	————
EDML	$7.72 \pm 0.09\,\mathrm{cm}$	$7.12 \pm 0.08\,\mathrm{cm}$	$8.9 \pm 0.3\,\mathrm{cm}^2$	$8.1 \pm 0.3\,\mathrm{cm}^2$	$7.1 \pm 0.2\,\mathrm{cm}^2$	1.18 ± 0.01
	$-42.8 \pm 0.9\,°\mathrm{C}$	$-42.5 \pm 0.9\,°\mathrm{C}$	$-44.6 \pm 1.1\,°\mathrm{C}$	$-45.9 \pm 1.0\,°\mathrm{C}$	$-47.6 \pm 1.0\,°\mathrm{C}$	$-32.4 \pm 3.1\,°\mathrm{C}$
NEEM	$7.98 \pm 0.22\,\mathrm{cm}$	$7.20 \pm 0.32\,\mathrm{cm}$	$11.8 \pm 1.6\,\mathrm{cm}^2$	$10.2 \pm 1.1\,\mathrm{cm}^2$	$4.5 \pm 2.0\,\mathrm{cm}^2$	1.23 ± 0.05
	$-31.8 \pm 1.1\,°\mathrm{C}$	$-32.4 \pm 1.4\,°\mathrm{C}$	$-28.4 \pm 2.6\,°\mathrm{C}$	$-30.7 \pm 2.1\,°\mathrm{C}$	$-45.9 \pm 10.1\,°\mathrm{C}$	$-49.3 \pm 15.0\,°\mathrm{C}$
NGRIP	$8.65 \pm 0.22\,\mathrm{cm}$	————	————	————	————	————
	$-31.6 \pm 1.1\,°\mathrm{C}$	————	————	————	————	————
Dome F	$5.76 \pm 0.15\,\mathrm{cm}$	$4.92 \pm 0.06\,\mathrm{cm}$	$9.0 \pm 1.8\,\mathrm{cm}^2$	$5.4 \pm 0.8\,\mathrm{cm}^2$	$4.4 \pm 1.9\,\mathrm{cm}^2$	1.37 ± 0.08
	$-57.6 \pm 1.0\,°\mathrm{C}$	$-58.5 \pm 0.8\,°\mathrm{C}$	$-54.2 \pm 2.8\,°\mathrm{C}$	$-60.4 \pm 2.2\,°\mathrm{C}$	$-63.7 \pm 5.7\,°\mathrm{C}$	$-80.9 \pm 14.0\,°\mathrm{C}$
Dome C	$6.97 \pm 0.15\,\mathrm{cm}$	$6.34 \pm 0.08\,\mathrm{cm}$	$8.4 \pm 1.9\,\mathrm{cm}^2$	$6.7 \pm 1.1\,\mathrm{cm}^2$	$0.4 \pm 0.4\,\mathrm{cm}^2$	1.21 ± 0.05
	$-52.8 \pm 1.0\,°\mathrm{C}$	$-52.5 \pm 0.9\,°\mathrm{C}$	$-54.3 \pm 3.0\,°\mathrm{C}$	$-56.9 \pm 2.3\,°\mathrm{C}$	$-88.8 \pm 5.9\,°\mathrm{C}$	$-42.8 \pm 18.4\,°\mathrm{C}$
GRIP early	$9.31 \pm 0.24\,\mathrm{cm}$	$8.25 \pm 0.09\,\mathrm{cm}$	$18.7 \pm 4.0\,\mathrm{cm}^2$	$20.4 \pm 1.9\,\mathrm{cm}^2$	$6.6 \pm 1.1\,\mathrm{cm}^2$	1.27 ± 0.06
	$-28.2 \pm 1.2\,°\mathrm{C}$	$-29.4 \pm 1.0\,°\mathrm{C}$	$-21.5 \pm 4.4\,°\mathrm{C}$	$-19.6 \pm 2.1\,°\mathrm{C}$	$-38.4 \pm 2.7\,°\mathrm{C}$	$-60.9 \pm 16.4\,°\mathrm{C}$
NEEM dis	$10.33 \pm 0.19\,\mathrm{cm}$	$9.72 \pm 0.20\,\mathrm{cm}$	$12.1 \pm 1.8\,\mathrm{cm}^2$	$10.0 \pm 0.9\,\mathrm{cm}^2$	$1.6 \pm 0.2\,\mathrm{cm}^2$	1.13 ± 0.02
	$-25.9 \pm 1.1\,°\mathrm{C}$	$-25.5 \pm 1.1\,°\mathrm{C}$	$-29.3 \pm 2.7\,°\mathrm{C}$	$-32.3 \pm 1.8\,°\mathrm{C}$	$-59.2 \pm 2.0\,°\mathrm{C}$	$-4.2 \pm 18.3\,°\mathrm{C}$
NEEM CFA	$10.27 \pm 0.19\,\mathrm{cm}$	$9.65 \pm 0.18\,\mathrm{cm}$	$12.3 \pm 1.1\,\mathrm{cm}^2$	$11.4 \pm 0.9\,\mathrm{cm}^2$	$11.2 \pm 0.6\,\mathrm{cm}^2$	1.13 ± 0.01
	$-26.1 \pm 1.1\,°\mathrm{C}$	$-25.7 \pm 1.1\,°\mathrm{C}$	$-29.0 \pm 1.8\,°\mathrm{C}$	$-30.1 \pm 1.7\,°\mathrm{C}$	$-30.4 \pm 1.4\,°\mathrm{C}$	$-5.7 \pm 14.2\,°\mathrm{C}$
NGRIP I	$9.68 \pm 0.16\,\mathrm{cm}$	————	————	————	————	————
	$-29.0 \pm 1.1\,°\mathrm{C}$	————	————	————	————	————
NGRIP II	$10.14 \pm 0.17\,\mathrm{cm}$	————	————	————	————	————
	$-27.8 \pm 1.0\,°\mathrm{C}$	————	————	————	————	————

6 DISCUSSION

6.1 Synthetic data

Based on the results of the sensitivity experiment with synthetic data, the following can be inferred. Firstly, the three techniques based on the single isotope diffusion, perform similarly and of all the techniques tested, yield the highest precision with a $s_{\bar{T}} \approx 1.0\,°\mathrm{C}$. Additionally, the estimated temperatures
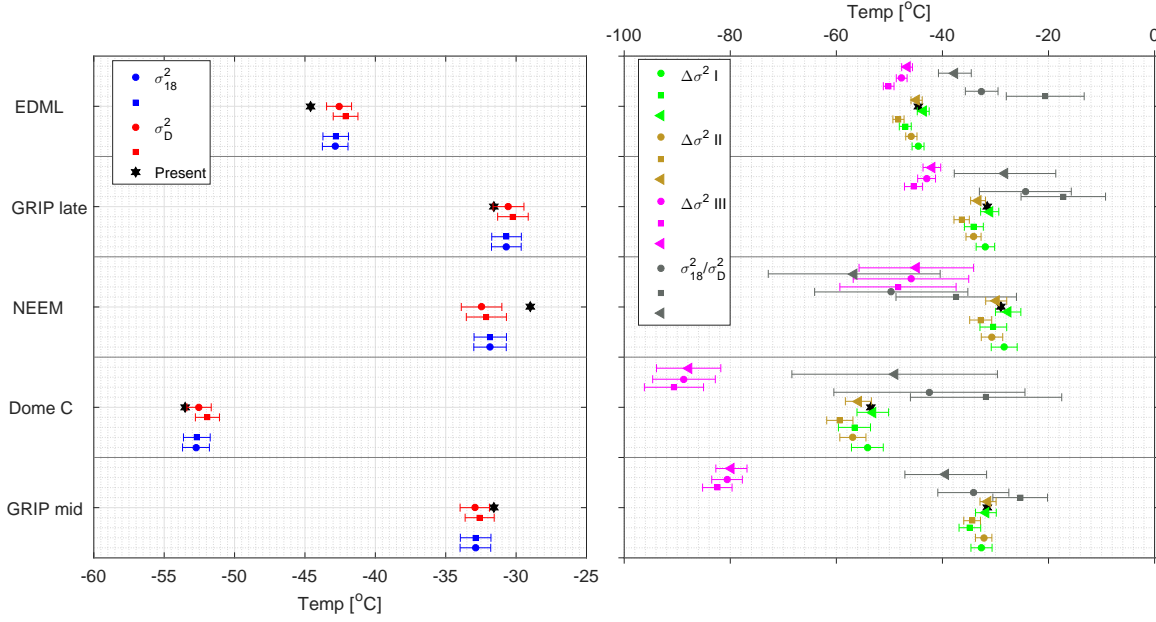
Figure 5.4: Temperature reconstructions based on different fractionation factor parametrizations. The left figure shows the single isotopologue methods and the right figure shows the dual isotope methods. The circles represent using the fractionation factors of Majoube (1970), Merlivat & Nief (1967), the squares represent Ellehoj et al. (2013) and the triangles represent Lamb et al. (2017), Majoube (1970).

425 $\overline{T}$ are within $1s_{\overline{T}}$ of the forcing temperature T_{sur}, a result pointing to a good performance with respect
426 to the accuracy of the temperature estimation.

427   The precision of the differential diffusion techniques is slightly inferior to single diffusion with the
428 subtraction technique being the least precise of all three differential diffusion approaches ($s_{\overline{T}} \approx 2.6\,^\circ$C).
429 A possible reason for this result may be the fact that the subtraction technique relies on the tuning
430 of 8 optimization parameters as described in Sec. 4.1 and 4.2. Both the linear fit and the correlation
431 techniques yield precision estimates of $1.8\,^\circ$C and $1.3\,^\circ$C, respectively. Despite the high precision of
432 the correlation technique, the tests shows that the technique has a bias toward colder temperatures. The
433 linear fit is therefore the most optimal of the differential diffusion techniques. All 10 experiments utilizing
434 differential diffusion methods, yield an accuracy that lies within the $2s_{\overline{T}}$ range ($1s_{\overline{T}}$ range for 9 out of
435 10 experiments). We can conclude that experiments involving the estimation of the diffusion length ratio
436 indicate that the latter are practically unusable due to very high uncertainties with $s_{\overline{T}}$ averaging to a value
437 of $\approx 16\,^\circ$C for all four experiments. A general trend that seems to be apparent for all the experiments,
438 is that the results for the case A forcing yield slightly lower uncertainties when compared to those for

439 the case B forcing, likely indicating a temperature and accumulation influence in the performance of all
440 the reconstruction techniques.

441 *6.2 Ice core data*

442   The precision $s_{\bar{T}}$ of each reconstruction technique has been quantified by averaging the squared standard
443 deviations of the reconstructed temperatures (Table 5.3). In accordance with the results from the synthetic
444 data test, the most precise reconstructions are obtained when using the single isotope diffusion methods.
445 The single diffusion methods have a $s_{\bar{T}}$ of $1.1\,^{\circ}\mathrm{C}$, while the differential diffusion methods $^{18}\Delta\sigma^2$ I, II
446 and III have a $s_{\bar{T}}$ of $2.6\,^{\circ}\mathrm{C}$, $1.9\,^{\circ}\mathrm{C}$ and $4.8\,^{\circ}\mathrm{C}$, respectively. The correlation-based technique is hereby
447 shown to be the least precise differential diffusion method. This differs from the result of the synthetic
448 data, where the correlation-based technique had the most precise results. Of the differential diffusion
449 methods, the linear fit of the logarithmic ratio provides the most precise results, with a precision similar
450 to that found from the synthetic data (Sec. 6.1). Of all the tested techniques, the diffusion length ratio
451 method is the least precise with a $s_{\bar{T}}$ of $11.8\,^{\circ}\mathrm{C}$. A similar precision was found from the synthetic data.
452   It is not possible to quantify the accuracy of the methods when applied on short ice core data sections,
453 as the reconstructed temperatures represent the integrated firn column temperature. The reconstructed
454 temperatures should therefore not necessarily be completely identical to present day annual temperatures.
455 However, clear outliers can still be inferred from the data as temperature estimates that deviate with
456 $-30\,^{\circ}\mathrm{C}$ from the present day annual mean temperatures are unrealistic. Alternately, the root-mean-square
457 deviation (RMSD) has been calculated in order to quantify the consistency between the reconstructed
458 temperatures of any two methods (x and y):

$$\mathrm{RMSD} = \sqrt{\frac{\sum_{j=1}^{n}\left(x_j - y_j\right)^2}{n}}, \tag{6.1}$$

459 where j represents the drill site and n the total number of sites.

460   First we address the correlation-based and diffusion length ratio techniques as these two methods
461 result in temperatures that clearly deviate with present day annual mean temperatures. Besides the low
462 precision of the diffusion length ratio method, its temperature esimates are highly inconsistent with the
463 results of the other techniques, with RMSDs varying from $21\,^{\circ}\mathrm{C}$ to $34\,^{\circ}\mathrm{C}$. For the correlation-based
464 technique, similar high RMSDs are found between the temperature estimates of the $^{18}\Delta\sigma^2$ I and III, and
465 the $^{18}\Delta\sigma^2$ II and III techniques. Here, the RMSDs are found to be $24.6\,^{\circ}\mathrm{C}$ and $23.5\,^{\circ}\mathrm{C}$, respectively.
466 A high RMSD ($24.5\,^{\circ}\mathrm{C}$) is also found when comparing the temperature estimates originating from the
467 σ_{18}^2 and $^{18}\Delta\sigma^2$ III methods. The large differences between the correlation-based and spectral-based
468 temperature estimates are particularly pronounced for GRIP, NEEM (Fig. 5.2), Dome C and the discretely

measured NEEM section (Fig. 5.3). In addition, it can be seen that the correlation-based method results in significantly different temperatures for the discretely and continuously measured NEEM section. A similar difference is not found from the spectral-based methods. Instead, these provide consistent temperatures independent of the processing scheme. The generally poor performance of the correlation-based method on ice core data contradicts the high accuracy and precision of the synthetic reconstructions, and is most likely caused by an oversimplification of the relationship between δD and δ^{18}O. The generation of the synthetic data is based on the assumption that $\delta\mathrm{D} = 8 \cdot \delta^{18}\mathrm{O} + 10\text{\textperthousand}$. However, this premise neglects the time dependent $\mathrm{d_{xs}}$ signal. The correlation-based method can therefore be used to accurately reconstruct synthetic temperatures, while the accuracy and precision are much lower for ice core data, as such data has been influenced by the $\mathrm{d_{xs}}$ signal. In addition, these temperature estimates have been shown to be dependent on the sampling process. The correlation-based method therefore yields uncertain estimates of the differential diffusion length.

The temperature estimates originating from the σ_{18}^2 and σ_{D}^2 methods are found to have a RMSD of $0.7\,^\circ$C. This shows that the σ_{18}^2 and σ_{D}^2 methods result in similar temperatures, which is consistent with the high accuracies found from the synthetic data test. The temperature estimates of the $^{18}\Delta\sigma^2$ I method is similar to the present day annual temperature in six out of nine cases. However, the results of the $^{18}\Delta\sigma^2$ I and II techniques have a RMSD of $3.8\,^\circ$C. The seemingly accurate performance of the $^{18}\Delta\sigma^2$ I method could be either a coincidence or correct. It is difficult to select the most accurate results as both of the differential diffusion techniques before performed well in the accuracy test with the synthetic data. One should therefore not have a preferred technique without utilizing both methods on longer ice core sections. Basically, the reconstructed temperatures could be similar when the temperatures have been averaged over a longer record. Besides the internal differences in the results of the differential techniques, most of the temperature estimates do not match the results of the single diffusion lengths. This is clear from the RMSDs between the temperature estimates of the σ_{18}^2 and $^{18}\Delta\sigma^2$ I methods, and the σ_{18}^2 and $^{18}\Delta\sigma^2$ II methods which are found to be $3.9\,^\circ$C and $4.6\,^\circ$C, respectively.

We want to acknowledge that although the single diffusion length methods here provide the most precise results, the differential diffusion methods should still be superior in older glacial ice where ice diffusion dominates and the sample diffusion exceeds that of the spectral-based diffusion length. This does not apply in this study as we use ice core data from the Holocene period.

6.3 The fractionation factors

The temperature estimates resulting from the different fractionation factor parametrizations are shown in Fig. 5.4. For each method, the influence of the choice of parametrization on the reconstructed temperatures

has been quantified by calculating the RMSD between temperature estimates of two parametrizations. Comparing the parametrizations of Ellehoj et al. (2013) to those of Majoube (1970) and Merlivat & Nief (1967), the RMSDs of reconstructions that are based on the single diffusion lengths σ_{18}^2 and σ_D^2 are 0.04°C and 0.4°C. Thus, it is evident that the choice of fractionation factors has an insignificant effect on the results of the σ_{18}^2 method and a small effect on the results of the σ_D^2 method. The choice of parameterization has a greater effect on the temperatures of the $^{18}\Delta\sigma^2$ techniques, where the temperature estimate of the $^{18}\Delta\sigma^2$ I, II and III techniques have RMSDs of 2.3°C, 2.3°C and 2.2°C, respectively. Comparing the parametrization of Lamb et al. (2017) to that of Merlivat & Nief (1967), the temperatures of the $^{18}\Delta\sigma^2$ I, II and III techniques have RMSDs of 0.9°C, 0.9°C and 1.0°C, respectively. In general, smaller RMSDs are found when comparing with temperature estimates based on the Lamb et al. (2017) parametrization. For instance, comparing the temperatures of the σ_{18}^2/σ_D^2 technique based on Lamb et al. (2017) with those of Merlivat & Nief (1967), the σ_{18}^2/σ_D^2 technique yields a RMSD of 5.9°C, while the RMSD is 11.0°C when comparing the results based on the parametrizations of Ellehoj et al. (2013) with those of Majoube (1970) and Merlivat & Nief (1967). There are two reasons to why the RMSDs are smaller when comparing with the Lamb et al. (2017) parametrization: the parametrized α_D of Merlivat & Nief (1967) differs more with that of Ellehoj et al. (2013) than with that of Lamb et al. (2017), and the same α_{18} parametrization is used when comparing with Lamb et al. (2017).

The σ_{18}^2/σ_D^2 method is significantly more influenced by the fractionation factors. The high RMSDs imply that even if the diffusion length ratio is estimated with high confidence, the method is still too sensitive to the choice of parameterization. This makes the method less suitable as a paleoclimatic thermometer.

7 CONCLUSIONS

This study assessed the performance of six different diffusion-based temperature reconstruction techniques. By applying the methods on synthetic data, it was demonstrated that each method could be used to accurately reconstruct unbiased temperatures. Moreover, this approach facilitated precision estimates of each method. The precision of each technique was further quantified by utilizing every variety of the diffusion-based temperature proxy on thirteen high resolution data sets from Greenland and Antarctica. The results showed that the single diffusion length methods yielded similar temperatures and that they are the most precise of all the presented reconstruction techniques. The most precise of the three differential diffusion length techniques was the linear fit of the logarithmic ratio. The most uncertain way of reconstructing past temperatures was by employing the diffusion length ratio method. The results

from the correlation-based method were inconsistent to the results obtained through the spectral-based methods, and the method was considered to yield uncertain estimates of the differential diffusion length.

It was furthermore shown that the choice of fractionation factor parametrization only had a small impact on the results from the single diffusion length methods, while the influence was slightly higher for the differential diffusion length methods. The diffusion length ratio method was highly sensitive to the fractionation factor parametrization, and the method is not suitable as a paleoclimatic thermometer.

In conclusion, despite that the dual diffusion techniques seem to be the more optimal choices due to their independence of sampling and ice diffusion or densification and thinning processes, the uncertain estimates should outweigh the theoretical advantages. From the combined analyses of the synthetic data and ice core data, this study has demonstrated that methods based on the single isotope diffusion lengths result in the most accurate and precise estimates of past temperatures.

CO-AUTHORSHIP

CH and VG contributed equally to this work.

APPENDIX A

FIRN DIFFUSIVITY

562 We express the diffusivity as a function of firn density ρ and we use (Johnsen et al. 2000):

$$D(\rho) = \frac{m\,p\,D_{\mathrm{a}i}}{R\,T\,\alpha_{\mathrm{i}}\,\tau}\left(\frac{1}{\rho} - \frac{1}{\rho_{\mathrm{ice}}}\right). \tag{A.1}$$

563 The terms used in Eq. (A.1) and the parametrization used for them are described below:

564 • m: molar weight (kg)

565 • p: saturation vapor pressure over ice (Pa). We use (Murphy & Koop 2006):

$$p = \exp\left(9.5504 - \frac{5723.265}{T} + 3.530\,\ln(T) - 0.0073\,T\right) \tag{A.2}$$

566

567 • $D_{\mathrm{a}i}$: diffusivity of water vapor (for isotopologue i) in air ($\mathrm{m^2 s^{-1}}$). For the diffusivity of the abundant

568   isotopologue water vapor D_{a} we use (Hall & Pruppacher 1976):

$$D_{\mathrm{a}} = 2.1 \cdot 10^{-5}\left(\frac{T}{T_o}\right)^{1.94}\left(\frac{P_o}{P}\right) \tag{A.3}$$

569   with $P_{\mathrm{o}} = 1$ Atm, $T_{\mathrm{o}} = 273.15$ K and P, T the ambient pressure (Atm) and temperature (K).

570   Additionally from Merlivat & Jouzel (1979) $D_{a^2\mathrm{H}} = 0.9755 D_{\mathrm{a}}$ and $D_{a^{18}\mathrm{O}} = 0.9723 D_{\mathrm{a}}$ and from

571   Barkan & Luz (2007) $D_{a^{17}\mathrm{O}} = 0.98555 D_{\mathrm{a}}$.

572 • R: molar gas constant $R = 8.3144$ ($\mathrm{m^3 Pa K^{-1} mol^{-1}}$)

573 • T: Ambient temperature (K)

574 • α_{i}: Ice − Vapor fractionation factor. we use the formulations by Majoube (1970), Merlivat & Nief

575   (1967) and Barkan & Luz (2005) for $\alpha^2_{\mathrm{s/v}}$, $\alpha^{18}_{\mathrm{s/v}}$ and $\alpha^{17}_{\mathrm{s/v}}$ respectively.

$$\alpha_{\mathrm{Ice/Vapor}}\left(^2\mathrm{H}/^1\mathrm{H}\right) = 0.9098\,\exp(16288/T^2) \tag{A.4}$$

$$\alpha_{\mathrm{Ice/Vapor}}\left(^{18}\mathrm{O}/^{16}\mathrm{O}\right) = 0.9722\,\exp(11.839/T) \tag{A.5}$$

$$\alpha_{\mathrm{Ice/Vapor}}\left(^{17}\mathrm{O}/^{16}\mathrm{O}\right) = \exp\left(0.529\,\ln\left[\alpha_{\mathrm{Ice/Vapor}}\left(^{18}\mathrm{O}/^{16}\mathrm{O}\right)\right]\right) \tag{A.6}$$

576

577 • τ: The firn tortuosity. We use Schwander et al. (1988) as in Johnsen et al. (2000). More recent

578   results include Freitag et al. (2002) and Adolph & Albert (2014).

$$\frac{1}{\tau} = 1 - b \cdot \left(\frac{\rho}{\rho_{\mathrm{ice}}}\right)^2 \quad \rho \le \frac{\rho_{\mathrm{ice}}}{\sqrt{b}},\ b = 1.3 \tag{A.7}$$

579 Based on Eq. (A.7), $\tau \to \infty$ for $\rho > 804.3\,\mathrm{kg\,m^{-3}}$

APPENDIX B

THE FIRN TEMPERATURE PROFILE

Temperature variations in the firn column affect the amount of firn diffusion. The temperature profile T is modeled by solving the general heat transfer equation:

$$\frac{\partial T}{\partial t} = \kappa \frac{\partial^2 T}{\partial z^2} - \left(w - \left(\frac{\kappa}{\rho} + \frac{\partial \kappa}{\partial \rho} \right) \frac{\partial \rho}{\partial z} \right) \frac{\partial T}{\partial z}, \tag{B.1}$$

where ρ is the density, w is the vertical velocity and κ is the thermal diffusivity of firn. Here the internal heat production and the heat transport in the horizontal plane have been neglected. The thermal diffusivity of firn depends on density and the thermal diffusivity of ice (κ_{ice}) (Schwander et al. 1997):

$$\kappa = \kappa_{ice} \left(\frac{\rho}{\rho_i} \right)^{1 - 0.5(\rho/\rho_i)}, \tag{B.2}$$

where ρ_i is the density of ice. The thermal diffusivity of ice is defined as (Cuffey & Paterson 2010):

$$\kappa_{ice} = \frac{k}{\rho_i c_p} = \frac{9.828 \cdot \exp(-5.7 \cdot 10^{-3} T) \cdot 3.16 \cdot 10^7}{\rho_i (152.5 + 7.122T)}, \tag{B.3}$$

where c_p is the specific heat capacity and k is the thermal conductivity of ice. This allows for the computation of changes in thermal diffusivity with density:

$$\frac{\partial \kappa}{\partial \rho} = \kappa \left(\frac{1}{\rho} - \frac{1}{2\rho_i} \right) \left(1 + \ln \left(\frac{\rho}{\rho_i} \right) \right). \tag{B.4}$$

The surface temperature is parameterized as fluctuations around the mean annual temperature (T_{mean}) as in Simonsen et al. (2011):

$$T_{surf}(t) = T_{mean} + A \cos(bt) + B \cos(2bt), \tag{B.5}$$

where $A = 16.5$, $B = 3.0$ and $b = 0.5236$ are constants controlling the temperature amplitude and narrowness of the summer peak.

Figure B.1 shows the temperature variation a snow package experiences as it moves downwards. The seasonal temperature variation penetrates down to a depth of $10 - 12 \, \text{m}$. The heat equation is solved numerically by using a Crank-Nicolson scheme (Durran 2010).

APPENDIX C

ICE DIFFUSIVITY

The solid ice diffusivity parametrization we use in this study is based on Ramseier (1967) as it is consistent with previous studies. In this section we provide the reader with parametrizations from other studies. We assume an Arrhenius type relationship for the ice diffusivity of the form:

$$D_{\text{ice}} = D_o \exp \left(-\frac{X}{T} \right) \; [\text{m}^2\text{s}^{-1}]. \tag{C.1}$$
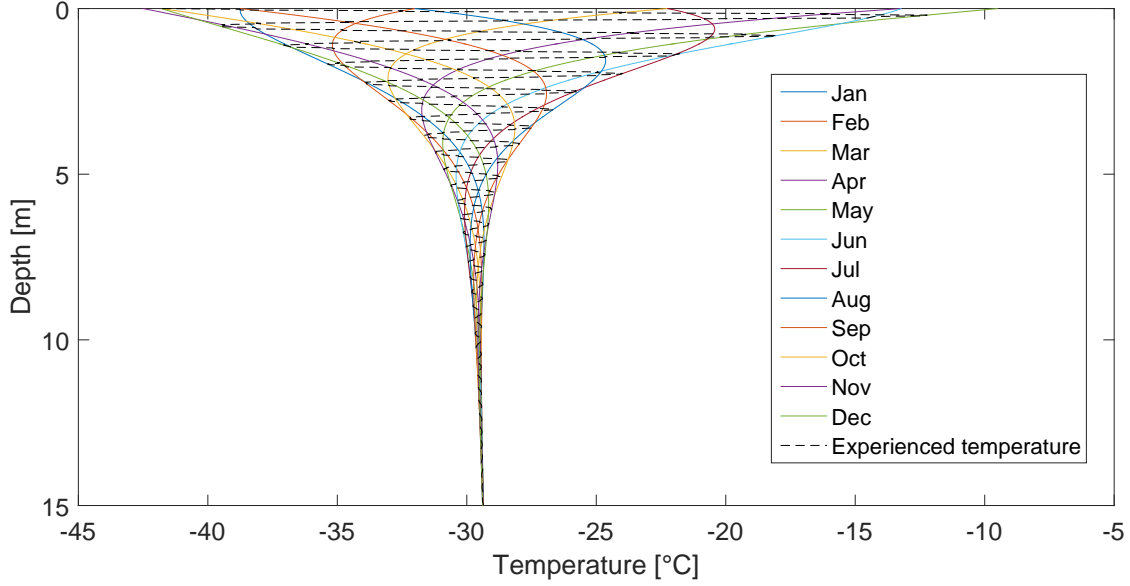
Figure B.1: Each solid colored line represent the temperature in one month of a year. The temperature a snow layer experiences as it moves down through the snow is represented by the black dashed line. The temperature is constant around 10-12 m. $T_{\mathrm{mean}} = -29\,^\circ\mathrm{C}$, $A = 0.22\ \mathrm{myr}^{-1}$ ice. eq.

In Eq. C.1, D_o is the pre-exponential factor in $\mathrm{m^2 s^{-1}}$ and X is the Arrhenius coefficient where $X = Q/R$ with Q being the activation energy in $\mathrm{kcal\,mol^{-1}}$ and R the universal gas constant $(8.314\ \mathrm{J K^{-1} mol^{-1}})$.

Results from four experimental studies are summarized in Table C.1. Together with the pre-exponential factors and the activation energies, we also evaluate the four different expressions of ice diffusivities for the temperature of $T = 245\mathrm{K}$.

When D_{ice} is known, a σ_{ice} calculation can be obtained by solving Eq. 2.5. Using the integrating factor $F = \exp\left(\int -2\dot{\varepsilon}_z\left(t\right)\mathrm{d}t\right)$ we get:

$$\frac{\mathrm{d}}{\mathrm{d}t}\left(\sigma_{\mathrm{ice}}^2\, e^{\int -2\dot{\varepsilon}_z(t)\mathrm{d}t}\right) = 2D_{\mathrm{ice}}\left(t\right)\, e^{\int -2\dot{\varepsilon}_z(t)\mathrm{d}t} \tag{C.2}$$

This finally yields the ice diffusion length for a layer with age t' that has undergone ice flow thinning $S(t')$:

$$\sigma_{\mathrm{ice}}^2\left(t'\right) = S\left(t'\right)^2 \int_0^{t'} 2D_{\mathrm{ice}}\left(t\right) S\left(t\right)^{-2}\ \mathrm{d}t \tag{C.3}$$

Table C.1: Four experimental studies with their estimated activation energies (Q), the pre-exponential factors (D_0), the activation energies (X), and the corresponding ice diffusivities for the temperature of $T = 245\,\mathrm{K}$ (D_{245}).

	$D_o\ [\mathrm{m^2 s^{-1}}]$	$Q\ [\mathrm{kcal mol^{-1}}]$	$X\ [\mathrm{K^{-1}}]$	$D_{245}\ [\mathrm{m^2 s^{-1}}]$
Ramseier (1967)	$9.2 \cdot 10^{-4}$	14.28	7186.5	$1.68 \cdot 10^{-16}$
Itagaki (1964)	0.014	14.97	7534.2	$6.18 \cdot 10^{-16}$
Blicks et al. (1966)	$2.5 \cdot 10^{-3}$	14.51	7302.4	$2.85 \cdot 10^{-16}$
Delibaltas et al. (1966)	$2.6 \cdot 10^{-3}$	15.66	7881.9	$2.83 \cdot 10^{-16}$

APPENDIX D

GENERATING SYNTHETIC DATA

The time series are generated using an AR-1 process with coefficient r_1 and variance ε

$$\delta_\mathrm{n} - r_1 \delta_\mathrm{n-1} = \varepsilon_\mathrm{n}. \tag{D.1}$$

For the AR-1 process we use $r_1 = 0.3$ and $\varepsilon = 120\,‰^2$ for case A and $200\,‰^2$ for case B. Each data section is 20 m long and has an initial spacing of $10^{-3}\,\mathrm{m}$. The $\delta\mathrm{D}$ and $\delta^{17}\mathrm{O}$ series are then generated assuming a $\mathrm{d_{xs}}$ signal of $10\,‰$ and an $\Delta^{17}\mathrm{O}$ signal of 0 per meg:

$$\delta\mathrm{D} = 8 \cdot \delta^{18}\mathrm{O} + 10‰ \tag{D.2}$$

$$\Delta^{17}\mathrm{O} = \ln(\delta^{17}\mathrm{O} + 1) - 0.528 \ln(\delta^{18}\mathrm{O} + 1) \tag{D.3}$$

The time series are then forward-diffused by means of numerical convolution with a Gaussian filter of variance σ^2_{input} equal to the diffusion length for every case (Table 5.1). This input diffusion length is calculated as:

$$\sigma^2_{input} = \sigma^2 \cdot \mathcal{S}^2 + \sigma^2_{ice}, \tag{D.4}$$

where σ^2 is the firn diffusion. For both case A and B, the ice diffusion is $\sigma_{ice} = 10^{-3}\,\mathrm{m}$ with a thinning of $\mathcal{S} = 0.80$. Sampling with a discrete scheme of $\Delta = 0.025\,\mathrm{m}$ and addition of white measurement noise completes the process of the time series generation. We use a noise level of $0.05\,‰$, $0.07\,‰$ and $0.5\,‰$ for $\delta^{17}\mathrm{O}$, $\delta^{18}\mathrm{O}$ and $\delta\mathrm{D}$ respectively, with the numbers being representative of measurement noise we have been observing over years of ice core measurements in our laboratory.

For a case B scenario, the sampled outputs of the synthetic data before and after diffusion is shown in Fig. D.1. Applying the forward-diffusion smoothens the large amplitudes of the high frequencies. This effect is further illustrated in Fig. D.2 which shows the PSD of the signal before and after diffusion.
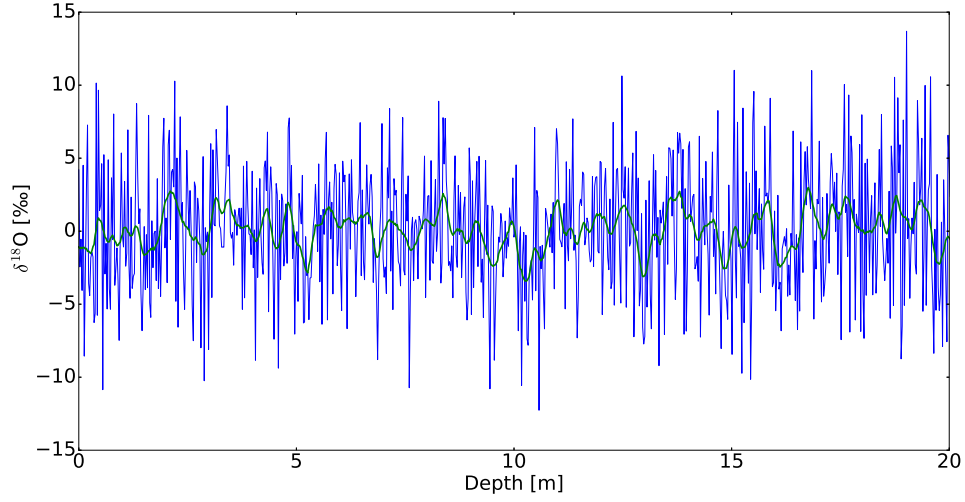
Figure D.1: Synthetic generated $\delta^{18}O$ series (case B) which both have been sampled. Blue curve represents the data before diffusion, and the green curve represents the data after diffusion. $\sigma = 8.4\,\text{cm}$.
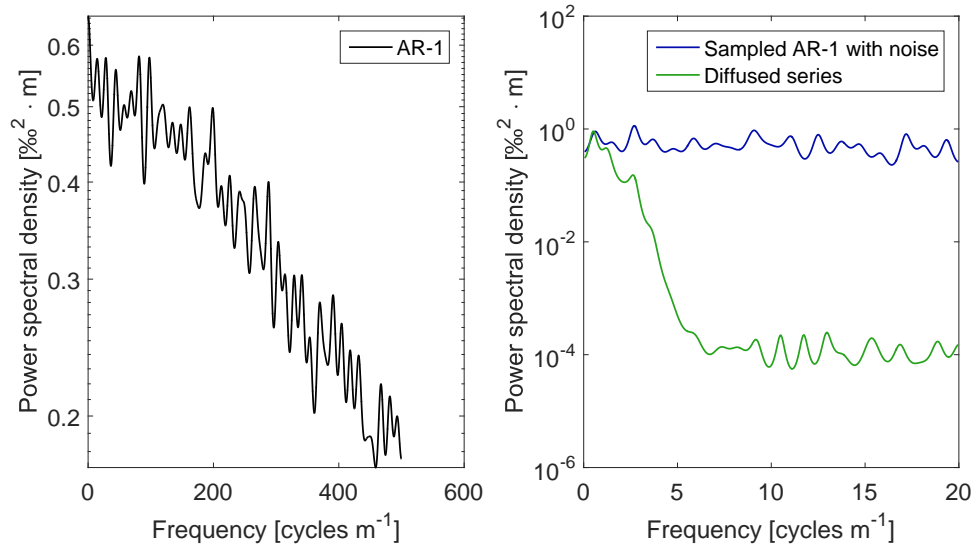

Figure D.2: Left: PSD of the raw AR-1 time series (case B $\delta^{18}O$ series). Right: PSD of the $\delta^{18}O$ series (from Fig. D.1). Blue curve represents the PSD of the sampled time series before diffusion, and the green curve represents the PSD of the sampled time series after diffusion.

APPENDIX E

DISCRETE SAMPLING DIFFUSION

The sample diffusion length σ_{dis} is estimated by setting the transfer function of a Gaussian filter equal to a rectangular filter with width of the sample size Δ. The transfer function for the Gaussian filter in Eq. 2.3 is found by its Fourier transform:

$$\mathfrak{F}\left[\mathcal{G}\right] = \hat{\mathcal{G}} = e^{-\frac{k^2 \sigma_{\text{dis}}^2}{2}}. \tag{E.1}$$

A regular rectangle function is defined as:

$$\text{rect(t)} = \begin{cases} 1 & \text{for } -\frac{1}{2} < t < \frac{1}{2} \\ \frac{1}{2} & \text{for } t = |\frac{1}{2}| \\ 0 & \text{for } t > |\frac{1}{2}| \end{cases} \tag{E.2}$$

This can be transformed into a rectangular function ($\Pi(t)$) with width Δ and amplitude A:

$$\Pi(t) = A \cdot \text{rect}(t \cdot \Delta), \quad \text{for } -\frac{\Delta}{2} < t < \frac{\Delta}{2}. \tag{E.3}$$

Normalization yields an amplitude of $A = 1/\Delta$. The Fourier transformation of the rectangular pulse is written as:

$$\hat{\Pi}(f) = \int_{-\infty}^{\infty} \Pi(t) e^{-2\pi i f t} \mathrm{d}t = \int_{-\Delta/2}^{\Delta/2} \frac{1}{\Delta} e^{-2\pi i f_{\text{Nq}} t} \mathrm{d}t, \tag{E.4}$$

where $f_{\text{Nq}} = 1/(2\Delta)$ is the Nyquist frequency. Setting equations E.1 and E.4 equal to each other:

$$e^{-\frac{k^2 \sigma_{dis}^2}{2}} = \int_{-\Delta/2}^{\Delta/2} \frac{1}{\Delta} e^{-2\pi i f_{nq} t} \mathrm{d}t, \tag{E.5}$$

where $k = 2\pi f_{\text{Nq}}$. This results in the following solution for the discrete sampling diffusion length:

$$\sigma_{\text{dis}}^2 = \frac{2\Delta^2}{\pi^2} \ln\left(\frac{\pi}{2}\right). \tag{E.6}$$

APPENDIX F

FIGURES

Here we provide figures that show the performance of each diffusion technique. For each data section we have the estimated uncorrected diffusion lengths in a table.
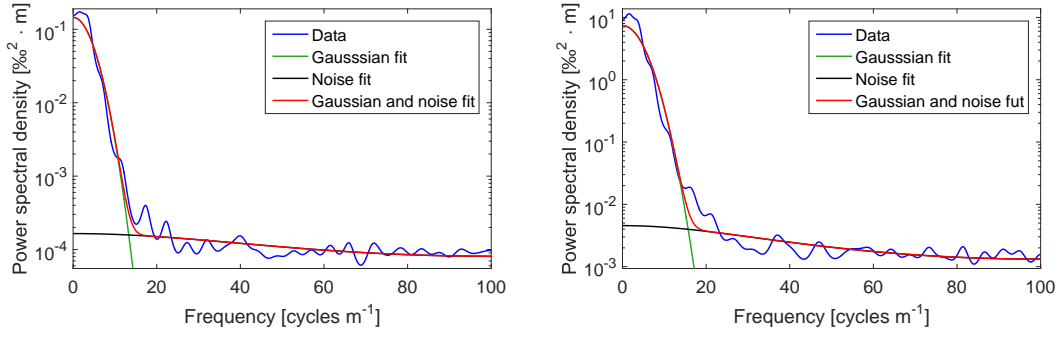
F.1 NEEM - late Holocene
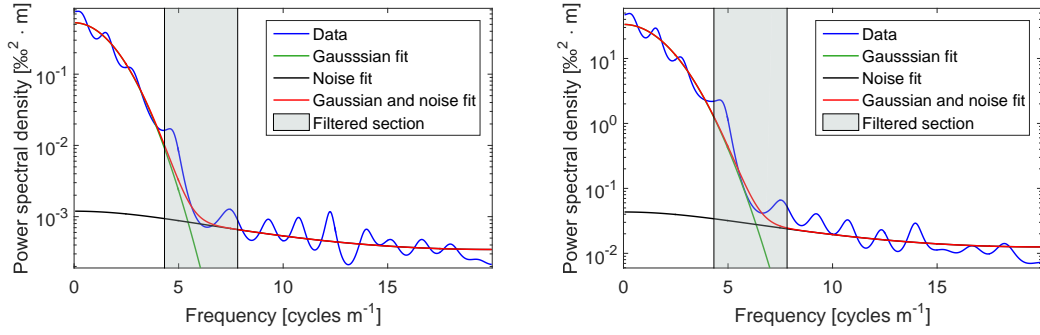
Figure F.1: NEEM. Late Holocene power spectra of $\delta^{18}O$ (left) and δD (right).

.
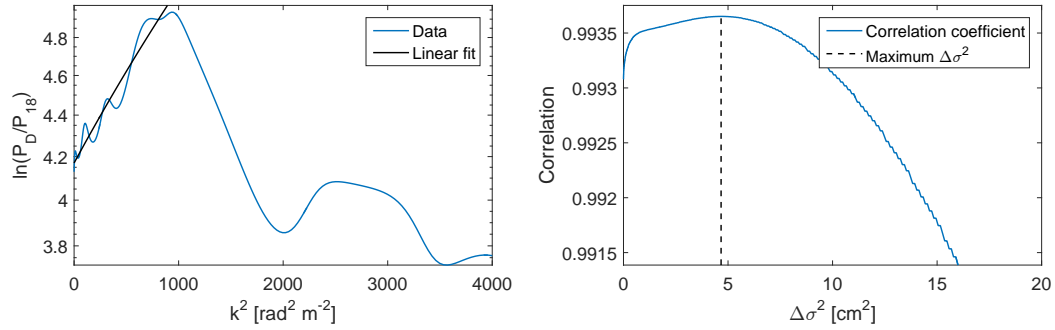
Figure F.2: Differential diffusion techniques applied on NEEM late Holocene data. Left: linear fit of the logarithmic PSD ratio ($^{18}\Delta\sigma^2$ II). Right: Correlation between $\delta^{18}O$ and artificially diffused δD ($^{18}\Delta\sigma^2$ III).

Table F.1: Estimated diffusion values for the NEEM late Holocene data. The values have not been corrected for sampling diffusion, ice diffusion and thinning.

σ_{18} [cm]	σ_{D} [cm]	$\Delta\sigma^2$ I [cm^2]	$\Delta\sigma^2$ [cm^2] II	$\Delta\sigma^2$ III [cm^2]
7.41	6.68	10.3	9.0	4.7

F.2 NEEM - CFA data section

Figure F.3: NEEM - CFA data. Early Holocene power spectra of δ^{18}O (left) and δD (right)
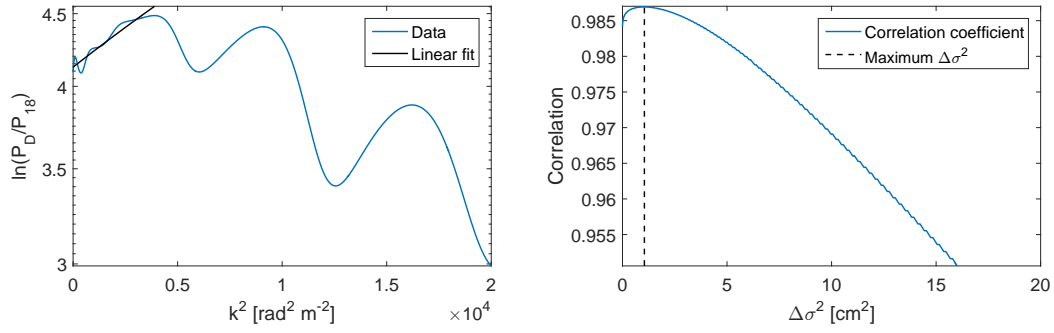
Figure F.4: Differential diffusion techniques applied on NEEM early Holocene CFA data. Left: linear fit of the logarithmic PSD ratio ($^{18}\Delta\sigma^2$ II). Right: Correlation between δ^{18}O and artificially diffused δD ($^{18}\Delta\sigma^2$ III).

Table F.2: Estimated values for NEEM early Holocene CFA data. The values have not been corrected for sampling diffusion, ice diffusion and thinning.

σ_{18} [cm]	σ_D [cm]	$\Delta\sigma^2$ I [cm^2]	$\Delta\sigma^2$ [cm^2] II	$\Delta\sigma^2$ III [cm^2]
3.12	2.78	2.0	1.1	1.0

F.3 NEEM - discrete data section
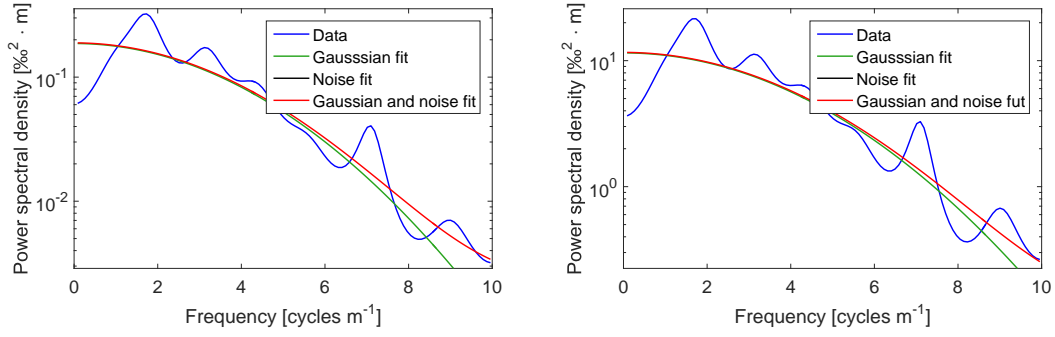
Figure F.5: NEEM - discrete data. Early Holocene power spectra of $\delta^{18}O$ (left) and δD (right)
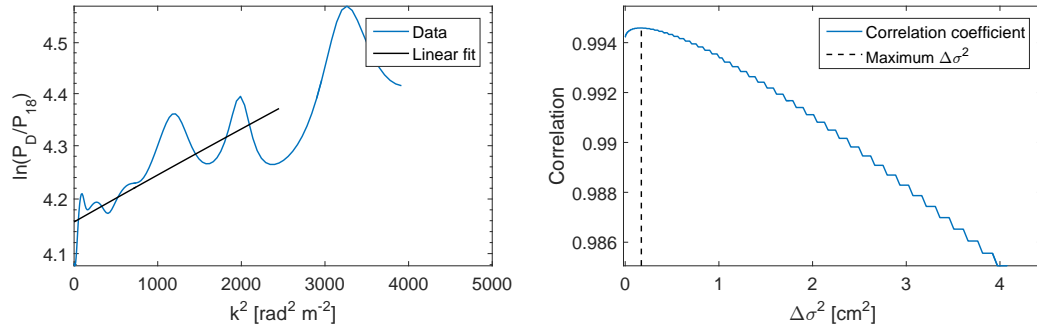
Figure F.6: Differential diffusion techniques applied on NEEM early Holocene discrete data. Left: linear fit of the logarithmic PSD ratio ($^{18}\Delta\sigma^2$ II). Right: Correlation between $\delta^{18}O$ and artificially diffused δD ($^{18}\Delta\sigma^2$ III).

Table F.3: Estimated values for NEEM early Holocene discrete data. The values have not been corrected for sampling diffusion, ice diffusion and thinning.

σ_{18} [cm]	σ_D [cm]	$\Delta\sigma^2$ I [cm^2]	$\Delta\sigma^2$ [cm^2] II	$\Delta\sigma^2$ III [cm^2]
3.58	3.35	1.6	0.9	0.2
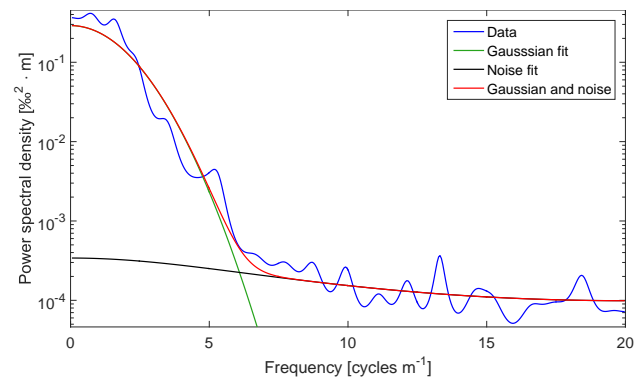
Figure F.7: NGRIP. Early Holocene power spectrum of δ^{18}O.

Table F.4: Estimated value for NGRIP late Holocene data. The value has not been corrected for sampling diffusion, ice diffusion and thinning.

σ_{18} [cm]	σ_D [cm]	$\Delta\sigma^2$ I [cm^2]	$\Delta\sigma^2$ [cm^2] II	$\Delta\sigma^2$ III [cm^2]
7.00	-	-	-	-
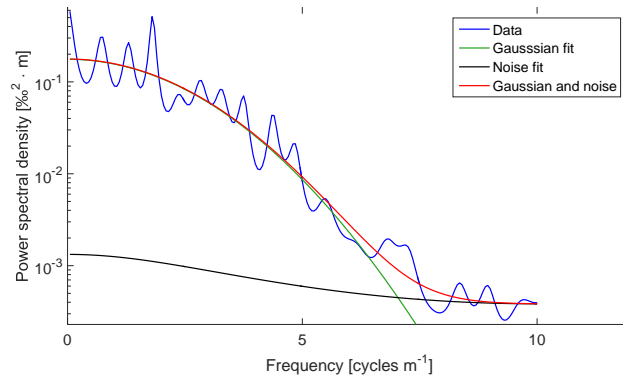
Figure F.8: NGRIP early Holocene core 1. Power spectrum of $\delta^{18}O$.

Table F.5: Estimated value for NGRIP early Holocene core 1 data. The value has not been corrected for sampling diffusion, ice diffusion and thinning.

σ_{18} [cm]	σ_D [cm]	$\Delta\sigma^2$ I [cm^2]	$\Delta\sigma^2$ [cm^2] II	$\Delta\sigma^2$ III [cm^2]
5.53	-	-	-	-
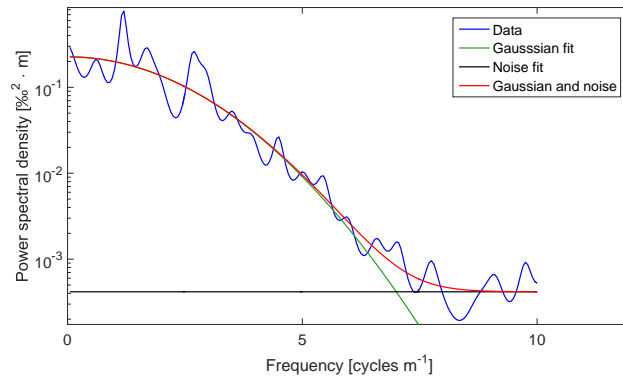
Figure F.9: NGRIP early Holocene core 2. Power spectrum of $\delta^{18}O$.

Table F.6: Estimated value for NGRIP early Holocene core 2 data. The value has not been corrected for sampling diffusion, ice diffusion and thinning.

σ_{18} [cm]	σ_D [cm]	$\Delta\sigma^2$ I [cm^2]	$\Delta\sigma^2$ [cm^2] II	$\Delta\sigma^2$ III [cm^2]
5.70	-	-	-	-
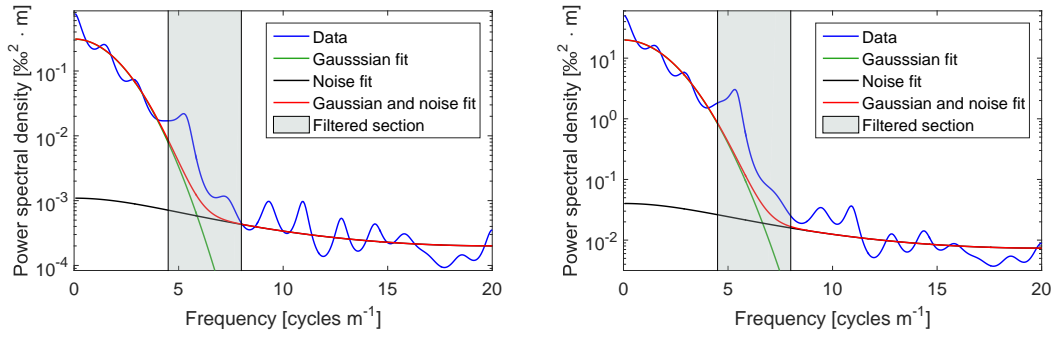
Figure F.10: GRIP. Late Holocene power spectra of δ^{18}O (left) and δD (right).
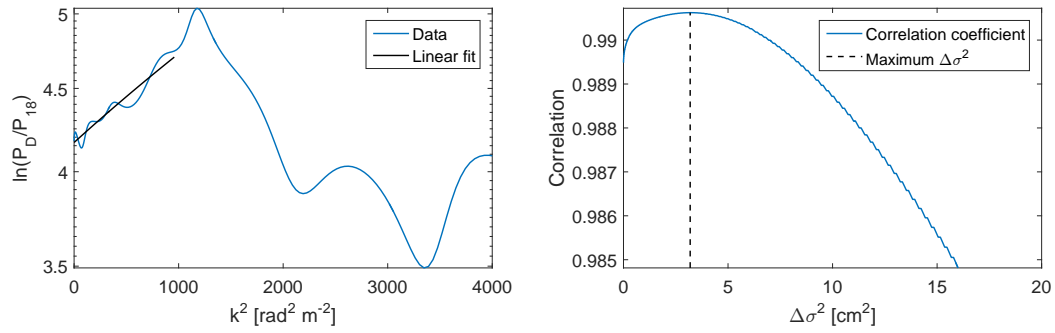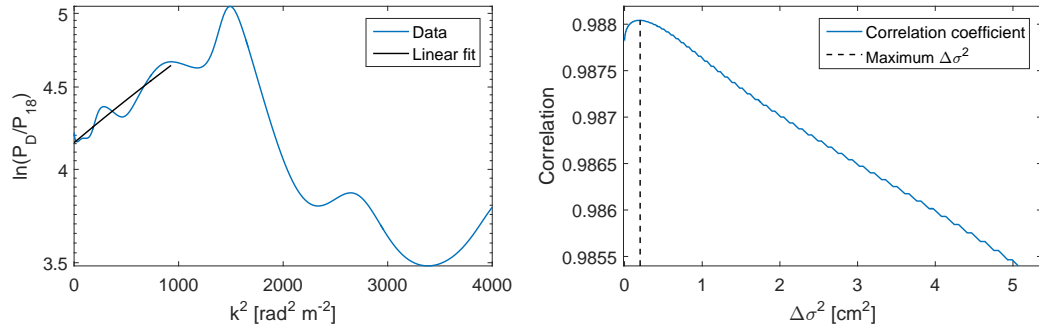

Figure F.11: Differential diffusion techniques applied on GRIP late Holocene data. Left: linear fit of the logarithmic PSD ratio ($^{18}\Delta\sigma^2$ II). Right: Correlation between δ^{18}O and artificially diffused δD ($^{18}\Delta\sigma^2$ III).

Table F.7: Estimated diffusion values for the GRIP late Holocene data. The values have not been corrected for sampling diffusion, ice diffusion and thinning.

| σ_{18} [cm]	σ_{D} [cm]	$\Delta\sigma^2$ I [cm^2]	$\Delta\sigma^2$ [cm^2] II	$\Delta\sigma^2$ III [cm^2]
6.78	6.31	6.2	5.6	3.2
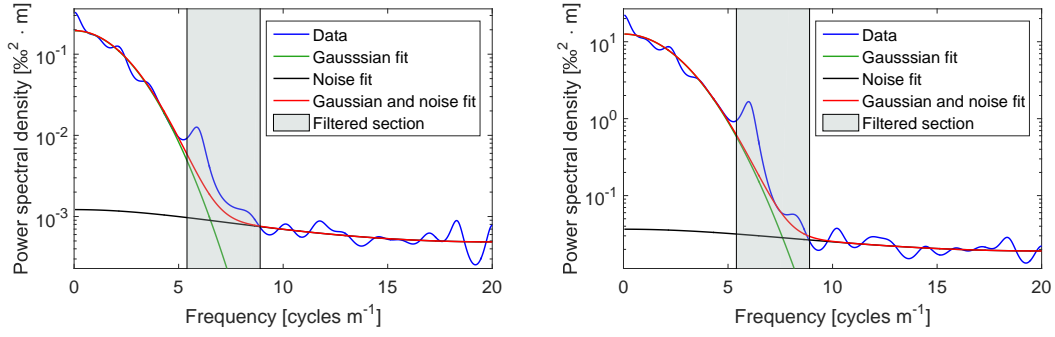
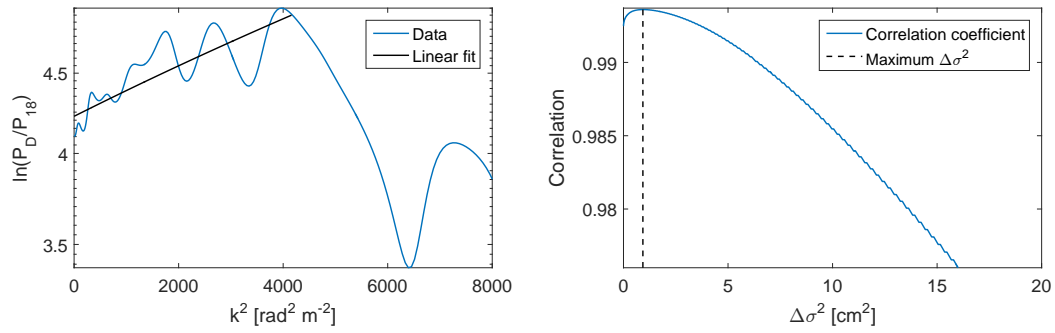Figure F.12: GRIP. Mid Holocene power spectra of δ^{18}O (left) and δD (right).

Figure F.13: Differential diffusion techniques applied on GRIP mid Holocene data. Left: linear fit of the logarithmic PSD ratio ($^{18}\Delta\sigma^2$ II). Right: Correlation between δ^{18}O and artificially diffused δD ($^{18}\Delta\sigma^2$ III).

Table F.8: Estimated diffusion values for the GRIP mid Holocene data. The values have not been corrected for sampling diffusion, ice diffusion and thinning.

σ_{18} [cm]	σ_D [cm]	$\Delta\sigma^2$ I [cm^2]	$\Delta\sigma^2$ [cm^2] II	$\Delta\sigma^2$ III [cm^2]
5.66	5.16	5.3	5.2	0.2
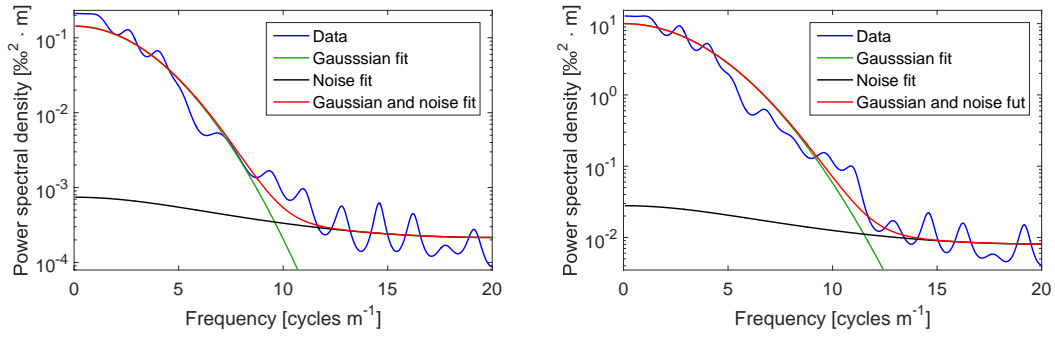
Figure F.14: GRIP. Early Holocene power spectra of δ^{18}O (left) and δD (right).

Figure F.15: Differential diffusion techniques applied on GRIP early Holocene data. Left: linear fit of the logarithmic PSD ratio ($^{18}\Delta\sigma^2$ II). Right: Correlation between δ^{18}O and artificially diffused δD ($^{18}\Delta\sigma^2$ III).

Table F.9: Estimated diffusion values for the GRIP early Holocene data. The values have not been corrected for sampling diffusion, ice diffusion and thinning.

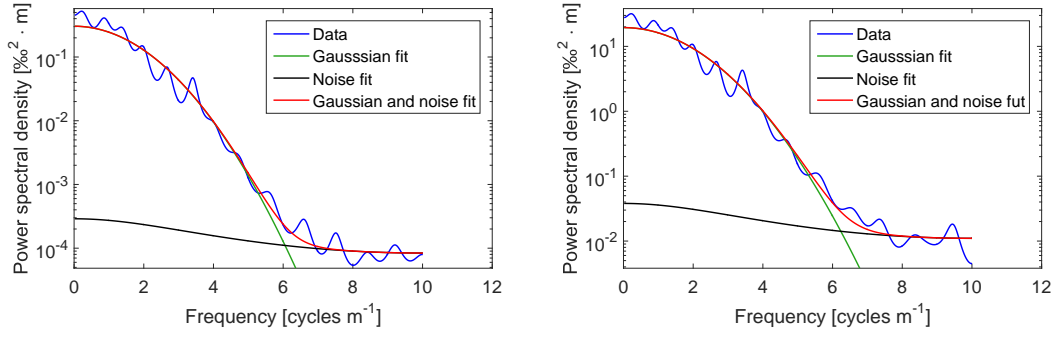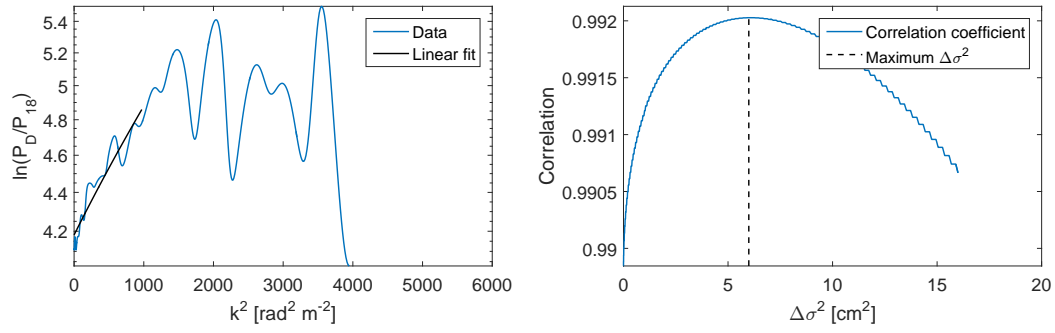| σ_{18} [cm]	σ_D [cm]	$\Delta\sigma^2$ I [cm^2]	$\Delta\sigma^2$ [cm^2] II	$\Delta\sigma^2$ III [cm^2]
4.07	3.61	3.5	1.6	0.9

Figure F.16: EDML. Power spectra of $\delta^{18}O$ (left) and δD (right).

Figure F.17: Differential diffusion techniques applied on EDML Holocene data. Left: linear fit of the logarithmic PSD ratio ($^{18}\Delta\sigma^2$ II). Right: Correlation between $\delta^{18}O$ and artificially diffused δD ($^{18}\Delta\sigma^2$ III).

Table F.10: Estimated diffusion values for the EDML data. The values have not been corrected for sampling diffusion, ice diffusion and thinning.

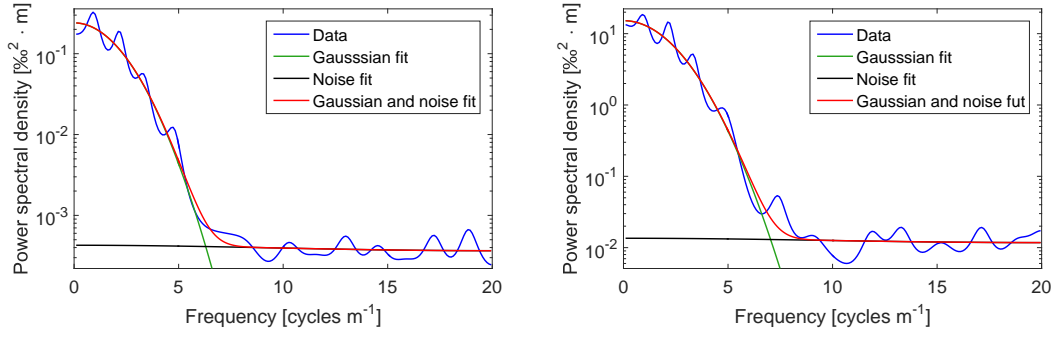| σ_{18} [cm]	σ_D [cm]	$\Delta\sigma^2$ I [cm^2]	$\Delta\sigma^2$ [cm^2] II	$\Delta\sigma^2$ III [cm^2]
7.40	6.86	7.7	7.0	6.0

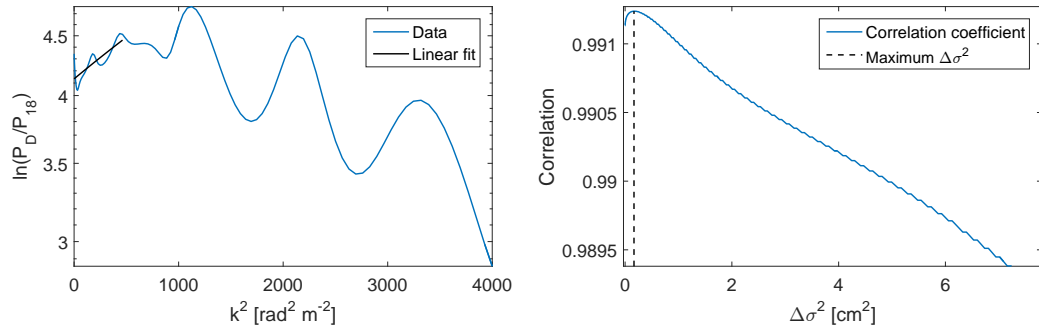Figure F.18: Dome C. Power spectra of $\delta^{18}O$ (left) and δD (right).

Figure F.19: Differential diffusion techniques applied on Dome C Holocene data. Left: linear fit of the logarithmic PSD ratio ($^{18}\Delta\sigma^2$ II). Right: Correlation between $\delta^{18}O$ and artificially diffused δD ($^{18}\Delta\sigma^2$ III).

Table F.11: Estimated diffusion values for the Dome C data. The values have not been corrected for sampling diffusion, ice diffusion and thinning.

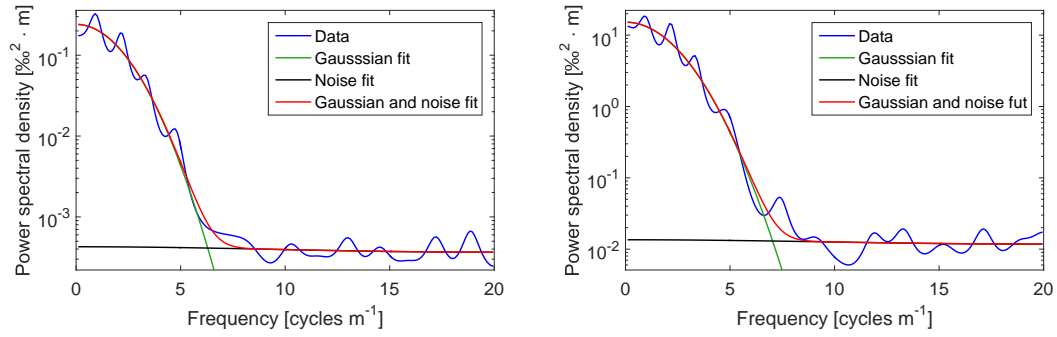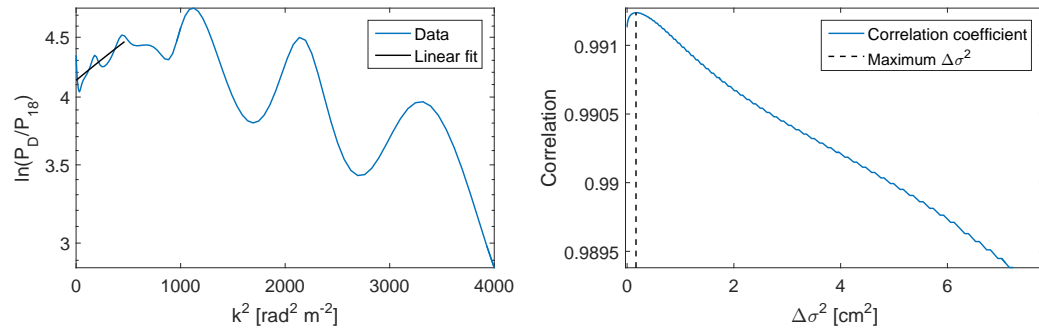| σ_{18} [cm]	σ_D [cm]	$\Delta\sigma^2$ I [cm^2]	$\Delta\sigma^2$ [cm^2] II	$\Delta\sigma^2$ III [cm^2]
6.38	6.01	4.6	7.1	0.2

Figure F.20: Dome F. Power spectra of δ^{18}O (left) and δD (right).

Figure F.21: Differential diffusion techniques applied on Dome F Holocene data. Left: linear fit of the logarithmic PSD ratio ($^{18}\Delta\sigma^2$ II). Right: Correlation between δ^{18}O and artificially diffused δD ($^{18}\Delta\sigma^2$ III).

Table F.12: Estimated diffusion values for the Dome F data. The values have not been corrected for sampling diffusion, ice diffusion and thinning.

σ_{18} [cm]	σ_{D} [cm]	$\Delta\sigma^2$ I [cm^2]	$\Delta\sigma^2$ [cm^2] II	$\Delta\sigma^2$ III [cm^2]
5.70	4.30	14.0	5.2	6.1

F.13 WAIS Divide

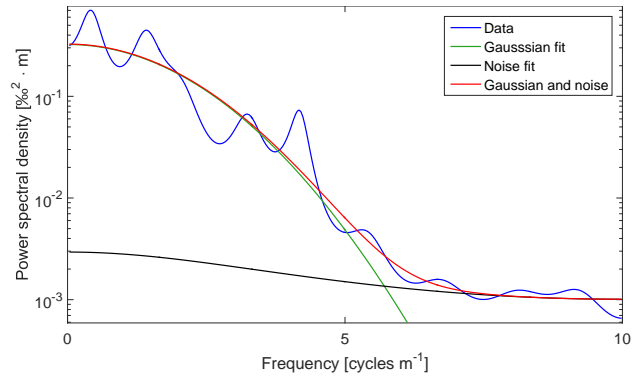
Figure F.22: WAIS D. Holocene power spectra of δ^{18}O.

Table F.13: Estimated value for WAIS D Holocene data. The value has not been corrected for sampling diffusion, ice diffusion and thinning.

σ_{18} [cm]	σ_D [cm]	$\Delta\sigma^2$ I [cm^2]	$\Delta\sigma^2$ [cm^2] II	$\Delta\sigma^2$ III [cm^2]
6.52	-	-	-	-

REFERENCES

657 Abramowitz, M. & Stegun, I. A. (1964), *Handbook of Mathematical Functions with Formulas, Graphs,*
658   *and Mathematical Tables*, 9th edn, Dover.

659 Adolph, A. C. & Albert, M. R. (2014), 'Gas diffusivity and permeability through the firn column at
660   Summit, Greenland: measurements and comparison to microstructural properties', *The Cryosphere*
661   **8**, 319–328.

662 Andersen, N. (1974), 'On The Calculation Of Filter Coefficients For Maximum Entropy Spectral
663   Analysis', *Geophysics* **39**(1).

664 Baker, L., Franchi, I. A., Maynard, J., Wright, I. P. & Pillinger, C. T. (2002), 'A technique for the
665   determination of O-18/O-16 and O-17/O-16 isotopic ratios in water from small liquid and solid
666   samples', *Analytical Chemistry* **74**(7), 1665–1673.

667 Banta, J. R., McConnell, J. R., Frey, M. M., Bales, R. C. & Taylor, K. (2008), 'Spatial and temporal
668   variability in snow accumulation at the West Antarctic Ice Sheet Divide over recent centuries', *Journal*
669   *of Geophysical Research* **113**.

Barkan, E. & Luz, B. (2005), 'High precision measurements of O-17/O-16 and O-18/O-16 ratios in (H$_2$O)', *Rapid Communications In Mass Spectrometry* **19**(24), 3737–3742.

Barkan, E. & Luz, B. (2007), 'Diffusivity fractionations of (H$_2$O)-O-16/(H$_2$O)-O-17 and (H$_2$O)-O-16/(H$_2$O)-O-18 in air and their implications for isotope hydrology', *Rapid Communications In Mass Spectrometry* **21**(18), 2999–3005.

Begley, I. S. & Scrimgeour, C. M. (1997), 'High-precision δ^2H and δ^{18}O measurement for water and volatile organic compounds by continuous-flow pyrolysis isotope ratio mass spectrometry', *Analytical Chemistry* **69**(8), 1530–1535.

Bigeleisen, J., Perlman, M. L. & Prosser, H. C. (1952), 'Conversion of hydrogenic materials to hydrogen for isotopic analysis', *Analytical Chemistry* **24**(8), 1356–1357.

Blicks, H., Dengel, O. & Riehl, N. (1966), 'Diffusion von protonen (tritonen) in reinen und dotierten eis-einkristallen', *Physik Der Kondensiterten Materie* **4**(5), 375–381.

Brand, W. A., Geilmann, H., Crosson, E. R. & Rella, C. W. (2009), 'Cavity ring-down spectroscopy versus high-temperature conversion isotope ratio mass spectrometry; a case study on δ^2H and δ^{18}O of pure water samples and alcohol/water mixtures', *Rapid Communications in Mass Spectrometry* **23**(12), 1879–1884.

Craig, H. (1961), 'Isotopic Variations in Meteroric Water', *Science* **133**(3465), 1702–1703.

Crosson, E. R. (2008), 'A cavity ring-down analyzer for measuring atmospheric levels of methane, carbon dioxide, and water vapor', *Applied Physics B-Lasers And Optics* **92**(3), 403–408.

Cuffey, K. M., Alley, R. B., Grootes, P. M., Bolzan, J. M. & Anandakrishnan, S. (1994), 'Calibration Of the Delta-O-18 isotopic paleothermometer for central Greenland, using borehole temperatures', *Journal Of Glaciology* **40**(135), 341–349.

Cuffey, K. M. & Paterson, W. S. B. (2010), *The physics of glaciers*, 4th edn, Elsevier.

Dahl-Jensen, D., Mosegaard, K., Gundestrup, N., Clow, G. D., Johnsen, S. J., Hansen, A. W. & Balling, N. (1998), 'Past temperatures directly from the Greenland Ice Sheet', *Science* **282**(5387), 268–271.

Dansgaard, W. (1954), 'The ^{18}O-abundance in fresh water', *Geochimica et Cosmochimica Acta* **6**(5–6), 241–260.

Dansgaard, W. (1964), 'Stable isotopes in precipitation', *Tellus B* **16**(4), 436–468.

Dansgaard, W. & Johnsen, S. J. (1969), 'A flow model and a time scale for the ice core from Camp Century, Greenland', *Journal of Glaciology* **8**(53).

Delibaltas, P., Dengel, O., Helmreich, D., Riehl, N. & Simon, H. (1966), 'Diffusion von ^{18}O in eis-einkristallen', *Physik Der Kondensiterten Materie* **5**(3), 166–170.

Durran, D. R. (2010), *Numerical Methods for Fluid Dynamics*, Springer, 2nd. Edition.

Ellehoj, M. D., Steen-Larsen, H. C., Johnsen, S. J. & Madsen, M. B. (2013), 'Ice-vapor equilibrium fractionation factor of hydrogen and oxygen isotopes: Experimental investigations and implications for stable water isotope studies', *Rapid Communications in Mass Spectrometry* **27**, 2149–2158.

Emanuelsson, B. D., Baisden, W. T., Bertler, N. A. N., Keller, E. D. & Gkinis, V. (2015), 'High-resolution continuous-flow analysis setup for water isotopic measurement from ice cores using laser spectroscopy', *Atmos. Meas. Tech.* **8**(7), 2869–2883.

Epstein, S., Buchsbaum, R., Lowenstam, H. & Urey, H. (1951), 'Carbonate-water isotopic temperature scale', *Geological Society of America Bulletin* **62**(4), 417.

Freitag, J., Dorbrindt, U. & Kipfstuhl, S. (2002), 'A new method for predicting transport properties of polar firn with respect to gases on the pore space scale', *Ann. Glacio.* **35**, 538–544.

Gehre, M., Hoefling, R., Kowski, P. & Strauch, G. (1996), 'Sample preparation device for quantitative hydrogen isotope analysis using chromium metal', *Analytical Chemistry* **68**(24), 4414–4417.

Gkinis, V. (2011), High resolution water isotope data from ice cores, PhD thesis, University of Copenhagen.

Gkinis, V., Popp, T. J., Blunier, T., Bigler, M., Schupbach, S., Kettner, E. & Johnsen, S. J. (2011), 'Water isotopic ratios from a continuously melted ice core sample', *Atmospheric Measurement Techniques* **4**(11), 2531–2542.

Gkinis, V., Simonsen, S. B., Buchardt, S. L., White, J. W. C. & Vinther, B. M. (2014), 'Water isotope diffusion rates from the NorthGRIP ice core for the last 16,000 years - glaciological and paleoclimatic implications', *Earth and Planetary Science Letters* **405**.

Guillevic, M., Bazin, L., Landais, A., Kindler, P., Orsi, A., Masson-Delmotte, V., Blunier, T., Buchardt, S. L., Capron, E., Leuenberger, M. ., Martinerie, P., Prie, F. & Vinther, B. M. (2013), 'Spatial gradients of temperature, accumulation and δ^{18}O-ice in Greenland over a series of Dansgaard-Oeschger events', *Climate of the Past* **9**, 1029–1051.

Hall, W. D. & Pruppacher, H. R. (1976), 'The Survival of Ice Particles Falling from Cirrus Clouds in Subsaturated Air', *Journal of the Atmospheric Sciences* **33**(10), 1995–2006.

Itagaki, K. (1964), 'Self-diffusion in single crystals of ice', *J. Phys. Soc. Jpn.* **19**(6), 1081–1081.

Johnsen, S., Clausen, H. B., Cuffey, K. M., Hoffmann, G., Schwander, J. & Creyts, T. (2000), 'Diffusion of stable isotopes in polar firn and ice: the isotope effect in firn diffusion', *Physics of Ice Core Records* pp. 121–140.

Johnsen, S. J. (1977), 'Stable Isotope Homogenization of Polar Firn and Ice', *Isotopes and Impurities in Snow and Ice* pp. 210–219.

Johnsen, S. J., Dahl Jensen, D., Dansgaard, W. & Gundestrup, N. (1995), 'Greenland paleotemperatures

derived from GRIP bore hole temperature and ice core isotope profiles', *Tellus B-Chemical And Physical Meteorology* **47**(5), 624–629.

Johnsen, S. J., Dahl-Jensen, D., Gundestrup, N., Steffensen, J. P., Clausen, H. B., Miller, H., Masson-Delmotte, V., Sveinbjrnsdottir, A. E. & White, J. (2001), 'Oxygen isotope and palaeotemperature records from six Greenland ice-core stations: Camp Century, Dye-3, GRIP, GISP2, Renland and NorthGRIP', *Journal of Quaternary Science* **16**(4).

Johnsen, S. J. & White, J. (1989), 'The origin of Arctic precipitation under present and glacial conditions', *Tellus* **41B**, 452–468.

Jones, T. R., White, J. W. C., Steig, E. J., Vaughn, B. H., Morris, V., Gkinis, V., Markle, B. R. & Schoenemann, S. W. (2017), 'Improved methodologies for continuous-flow analysis of stable water isotopes in ice cores', *Atmos. Meas. Tech* **10**, 617–632.

Jouzel, J., Alley, R. B., Cuffey, K. M., Dansgaard, W., Grootes, P., Hoffmann, G., Johnsen, S. J., Koster, R. D., Peel, D., Shuman, C. A., Stievenard, M., Stuiver, M. & White, J. (1997), 'Validity of the temperature reconstruction from water isotopes in ice cores', *Journal Of Geophysical Research-Oceans* **102**(C12), 26471–26487.

Jouzel, J. & Merlivat, L. (1984), 'Deuterium and oxygen 18 in precipitation: modeling of the isotopic effects during snow formation', *Journal of Geophysical Research-Atmospheres* **89**(D7), 11749 – 11759.

Kawamura, K., Nakazawa, T., Aoki, S., Sugawara, S., Fujii, Y. & Watanabe, O. (2003), 'Atmospheric CO_2 variations over the last three glacial-interglacial climatic cycles deduced from the Dome Fuji deep ice core, Antarctica using a wet extraction technique', *Tellus* **55B**, 126–137.

Kay, S. M. & Marple, S. L. (1981), 'Spectrum Analysis - A Modern Perspective', *Proceedings of the IEEE* **69**(11).

Lamb, K. D., Clouser, B. W., Bolot, M., Sarkozy, L., Ebert, V., Saathoff, H., Möhler, O. & Moyer, E. J. (2017), 'Laboratory measurements of HDO/H_2O isotopic fractionation during ice deposition in simulated cirrus clouds'.

Livingston, F. E., Whipple, G. C. & George, S. M. (1997), 'Diffusion of HDO into single-crystal (H_2O)-O-16 ice multilayers: Comparison with (H_2O)-O-18', *Journal of Physical Chemistry B* **101**(32), 6127–6131.

Lorius, C., Merlivat, L., Jouzel, J. & Pourchet, M. (1979), 'A 30,000-yr isotope climatic record from Antarctic ice', *Nature* **280**, 644 – 648.

Majoube, M. (1970), 'Fractionation factor of ^{18}O between water vapour and ice', *Nature* **226**(1242).

Meijer, H. A. J. & Li, W. J. (1998), 'The use of electrolysis for accurate delta O-17 and delta O-18 isotope measurements in water', *Isotopes In Environmental And Health Studies* **34**(4), 349–369.

Merlivat, L. & Jouzel, J. (1979), 'Global Climatic Interpretation of the Deuterium-Oxygen 18 Relationship for Precipitation', *Journal of Geophysical Research* **84**(8).

Merlivat, L. & Nief, G. (1967), 'Fractionnement Isotopique Lors Des Changements Detat Solide-Vapeur Et Liquide-Vapeur De Leau A Des Temperatures Inferieures A 0 Degrees C', *Tellus* **19**(1), 122–127.

Mook, J. (2000), *Environmental Isotopes in the Hydrological Cycle Principles and Applications*, International Atomic Energy Agency.

Murphy, D. M. & Koop, T. (2006), 'Review of the vapour pressures of ice and supercooled water for atmospheric applications', *Q.J.R. Meteorol. Soc.* **131**, 1539–1565.

NGRIP members (2004), 'High-resolution record of Northern Hemisphere climate extending into the last interglacial period', *Nature* **431**(7005), 147–151.

Oerter, H., Graf, W., Meyer, H. & Wilhelms, F. (2004), 'The EPICA ice core Droning Maud Land: first results from stable-isotope measurements', *Ann. Glaciol.* **39**, 307–312.

Press, W. H., Teukolsky, S. A., Vetterling, W. T. & Flannery, B. P. (2007), *Numerical Recipes: The Art of Scientific Computing*, Cambridge University Press.

Ramseier, R. O. (1967), 'Self-diffusion of tritium in natural and synthetic ice monocrystals', *Journal Of Applied Physics* **38**(6), 2553–2556.

Rasmussen, S. O., Abbott, P. M., Blunier, T., Bourne, A., Brook, E., Buchardt, S. L., Buizert, C., Chappellaz, J., Clausen, H. B., Cook, E., Dahl-Jensen, D., Davies, S. M., Guillevic, M., Kipfstuhl, S., Laepple, T., Seierstad, I. K., Severinghaus, J., Steffensen, J. P., Stowasser, C., Svensson, A., Vallelonga, P., Vinther, B. M., Wilhelms, F. & Winstrup, M. (2013), 'A first chronology for the North Greenland Eemian Ice Drilling (NEEM) ice core', *Climate of the Past* **9**, 2713–2730.

Rasmussen, S. O., Bigler, M., Blockley, S. P., Blunier, T., Buchardt, S. L., Clausen, H. B., Cvijanovic, I., Dahl-Jensen, D., Johnsen, S. J., Fischer, H., Gkinis, V., Guillevic, M., Hoek, W. Z., Lowe, J. J., Pedro, J. B., Popp, T., Seierstad, I. K., Steffensen, J. P. P., Svensson, A. M., Vallelonga, P., Vinther, B. M., Walker, M. J., Wheatley, J. J. & Winstrup, M. (2014), 'A stratigraphic framework for abrupt climatic changes during the last glacial period based on three synchronized greenland ice-core records: refining and extending the intimate event stratigraphy', *Quaternary Science Reviews* **106**, 14–28.

Schwander, J., Sowers, T., Barnola, J.-M., Blunier, T., Fuchs, A. & Malaiz, B. (1997), 'Age scale of the air in the summit ice: Implications for glacial-interglacial temperature change', *Journal of Geophysical Research* **102**(D16), 19,483 –19,493b.

Schwander, J., Stauffer, B. & Sigg, A. (1988), 'Air mixing in firn and the age of the air at pore close-off', *Annals of Glaciology* pp. 141 –145.

Severinghaus, J. P. & Brook, E. J. (1999), 'Abrupt climate change at the end of the last glacial period

inferred from trapped air in polar ice', *Science* **286**(5441), 930–934.

Severinghaus, J. P., Sowers, T., Brook, E. J., Alley, R. B. & Bender, M. L. (1998), 'Timing of abrupt climate change at the end of the Younger Dryas interval from thermally fractionated gases in polar ice', *Nature* **391**(6663), 141–146.

Simonsen, S. B., Johnsen, S. J., Popp, T. J., Vinther, B. M., Gkinis, V. & Steen-Larsen, H. C. (2011), 'Past surface temperatures at the NorthGRIP drill site from the difference in firn diffusion of water isotopes', *Climate of the Past* **7**.

Steig, E. J., Ding, Q., White, J. W. C., Kttel, M., Rupper, S. B., Neumann, T. A., Neff, P. D., Gallant, A. J. E., Mayewski, P. A., Taylor, K. C., Hoffmann, G., Dixon, D. A., Schoenemann, S., M., M. B., Schneider, D. P., Fudge, T. J., Schauer, A. J., Teel, R. P., Vaughn, B., Burgener, L., Williams, J. & Korotkikh, E. (2013), 'Recent climate and ice-sheet change in West Antarctica compared to the past 2000 years', *Nature Geoscience* **6**.

Steig, E. J., Gkinis, V., Schauer, A. J., Schoenemann, S. W., Samek, K., Hoffnagle, J., Dennis, K. J. & Tan, S. M. (2014), 'Calibrated high-precision 17O-excess measurements using cavity ring-down spectroscopy with laser-current-tuned cavity resonance', *Atmos. Meas. Tech.* **7**(8), 2421–2435.

Svensson, A., Fujita, S., Bigler, M., Braun, M., Dallmayr, R., Gkinis, V., Goto-Azuma, K., Hirabayashi, M., Kawamura, K., Kipfstuhl, S., Kjr, H. A., Popp, T., Simonsen, M., Steffensen, J. P., Vallelonga, P. & Vinther, B. M. (2015), 'On the occurrence of annual layers in Dome Fuji ice core early Holocene Ice', *Climate of the Past* **11**, 1127–1137.

van der Wel, G., Fischer, H., Oerter, H., Meyer, H. & Meijer, H. A. J. (2015), 'Estimation and calibration of the water isotope differential diffusion length in ice core records', *The Cryosphere* **9**(4), 1601–1616.

Vaughn, B. H., White, J. W. C., Delmotte, M., Trolier, M., Cattani, O. & Stievenard, M. (1998), 'An automated system for hydrogen isotope analysis of water', *Chemical Geology* **152**(3-4), 309–319.

Veres, D., Bazin, L., Landais, A., Kele, H. T. M., Lemieux-Dudon, B. B., Parrenin, F., Martinerie, P., Blayo, E., Blunier, T., Capron, E., Chappellaz, J., Rasmussen, S. O., Severi, M., Svensson, A., Vinther, B. & Wolff, E. W. (2013), 'The Antarctic ice core chronology (AICC2012): an optimized multi-parameter and multi-site dating approach for the last 120 thousand years', *Climate of the Past* **9**.

Vinther, B. M., Clausen, H. B., Johnsen, S. J., Rasmussen, S. O., Andersen, K. K., Buchardt, S. L., Dahl-Jensen, D., Seierstad, I. K., Siggaard-Andersen, M. L., Steffensen, J. P., Svensson, A., Olsen, J. & Heinemeier, J. (2006), 'A synchronized dating of three greenland ice cores throughout the holocene', *Journal Of Geophysical Research-Atmospheres* **111**(D13102).

Watanabe, O., Shoji, H., Satow, K and, M. H., Fujii, Y., Narita, H. & S., A. (2003), 'Dating of the Dome Fuji, Antarctica deep ice core', *Mem. Natl Inst. Polar Res., Spec. Issue* **57**, 25–37.

835   Whillans, I. M. & Grootes, P. M. (1985), 'Isotopic diffusion in cold snow and firn', *Journal of Geophysical*

836   *Research - Atmospheres* **90**, 3910–3918.